Indirect daylight oxidative degradation of polyethylene microplastics by a bio-waste modified TiO$_2$-based material

Paola Amato [a], Marzia Fantauzzi [b], Filomena Sannino [c,*], Ida Ritacco [d], Giuseppe Santoriello [d], Matteo Farnesi Camellone [e], Claudio Imparato [a], Aurelio Bifulco [a], Giuseppe Vitiello [a,f], Lucia Caporaso [d,*], Antonella Rossi [b,*], Antonio Aronne [a,*]

[a] Department of Chemical, Materials and Production Engineering, University of Naples Federico II, Piazzale V. Tecchio 80, I-80125 Naples, Italy
[b] Department of Chemical and Geological Sciences, University of Cagliari, Campus of Monserrato, I-09042 Monserrato, Cagliari, Italy
[c] Department of Agricultural Sciences, University of Naples Federico II, Via Università 100, I-80055 Portici, Naples, Italy
[d] Department of Chemistry and Biology "A. Zambelli", INSTM Research Unit, University of Salerno, I-84084 Fisciano, Salerno, Italy
[e] CNR-IOM, Consiglio Nazionale delle Ricerche – Istituto Officina dei Materiali, I-34136 Trieste, Italy
[f] CSGI, Center for Colloid and Surface Science, Via della Lastruccia 3, I-50019 Sesto Fiorentino, Florence, Italy

HIGHLIGHTS

- A new hybrid material (T-*Abi*) was synthesized by a waste-to-wealth approach.
- Rosin bio-waste acts as ligand to Ti^{4+} forming charge-transfer complex.
- O$_2^{\bullet-}$ radicals are generated on T-*Abi* without the need for any energetic source.
- A new oxidative degradation process using indirect daylight is exploited.
- After 1 month, alkanes, alcohols, esters are the LLDPE degradation by-products.

GRAPHICAL ABSTRACT
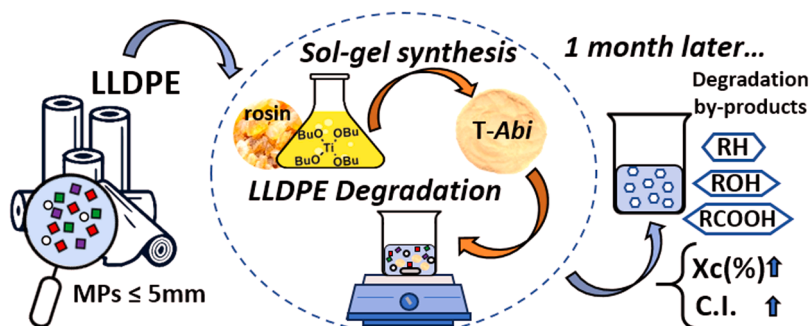
ARTICLE INFO

ABSTRACT

Microplastics are recognized as an emerging critical issue for the environment. Here an innovative chemical approach for the treatment of microplastics is proposed, based on an oxidative process that does not require any direct energy source (irradiation or heat). Linear low-density polyethylene (LLDPE) was selected as target commodity polymer, due to its widespread use, chemical inertness and inefficient recycling. This route is based on a hybrid material coupling titanium oxide with a bio-waste, rosin, mainly constituted by abietic acid, through a simple sol-gel synthesis procedure. The ligand-to-metal charge transfer complexes formed between rosin and Ti^{4+} allow the generation of reactive oxygen species without UV irradiation for its activation. In agreement with theorical calculations, superoxide radical ions are stabilized at ambient conditions on the surface of the hybrid TiO$_2$. Consequently, an impressive degradation of LLDPE is observed after 1 month exposure in a batch configuration under indirect daylight, as evidenced by the products revealed by gas chromatography-mass spectrometry analysis and by chemical and structural modifications of the polymer surface. In a context of

waste exploitation, this innovative and sustainable approach represents a promising cost-effective strategy for the oxidative degradation of microplastics, without producing any toxic by-products.

1. Introduction

The excellent chemical stability, the high durability and the low cost of plastics have determined their widespread usage in the world reaching, recently, a global annual production of about 380 million tons, 60 % of which are polyolefins. Considering 250 million tons of plastic wastes yearly produced, only 60 % of them are collected [1,2].

Plastics are persistent man-made pollutants and represent a global problem due to their ubiquitous presence and adverse effects on living organisms. Owing to ineffective recycling procedures, massive amounts of plastic wastes have accumulated in terrestrial and aquatic ecosystems, as landfilling is one of the most common solutions for end-of-life products. The largest amount of these wastes is composed by single-use plastics, mainly polyethylene and polypropylene, due to their use in the manufacturing of packaging, dining utensils, trash bags. Polyethylene accounts for up to 64 % of the waste generated from end-of-life synthetic plastics, causing white pollution [3–5]. Large amounts of plastic wastes that are not effectively recycled, incinerated for energy recovery, or properly disposed of in controlled landfills, are likely to disperse and accumulate in the environment. The breakdown of large plastics into microplastics (MPs) (particles size = 1 μm-5 mm) and nanoplastics (NPs) (particles size < 1 μm) [6] is affected by the physico-chemical properties of the polymers and the different environmental conditions like weathering, temperature, irradiation as well as pH. It is reported that by 2060, the proportion of MPs in the weight of global plastic pollutants will reach 13.2 % [7].

MPs with varied shapes, including beads, foams, fibers, and films [8–10], have been detected in air, aquatic system, river and ocean sediments as well as in soil [11–14]. The average abundance of MPs varied greatly among the different studied areas. In the European cities, the mean atmospheric MPs abundance from dry and wet deposition has been found between 118 (Paris) and 275 (Hamburg) particles $m^{-2} d^{-1}$ [15,16]. In the Midwest Pacific Ocean, the abundance of MPs ranged from 6028 to 95,335 pieces/km^2, with a mean concentration of 34,039 ± 25,101 pieces/km^2 [12]. Mulching soils contain larger amounts of MPs than non-mulching soils, with 571 pieces kg^{-1} and 263 pieces kg^{-1}, respectively, on average [14].

The fast release of MPs with their combined high resistance against degradation results in a rapid accumulation of these particles in the natural environment [9]. The chronic toxicity caused by long-term exposure to MPs poses a tremendous threat to biota and humans. MPs can enter in natural ecosystems easily through the food chain acting as ideal carriers of toxic organic and inorganic contaminants [17]. Particularly, due to the relatively large specific surface area of MPs, heavy metals [18] and persistent organic pollutants [19] may adhere and accumulate at the surface of MPs and then migrate into the environment.

Several technologies have been implemented to face this environmental emergency. Before entering the environment, wastewaters are treated in wastewater treatment plants (WWTPs), where the final stage, the tertiary treatment, exploits membrane bioreactor, sand filtration and dissolved air floatation. Despite the relative high MPs removal efficiency in WWTPs (98–99.9 %), the amount of MPs in the effluents can be reduced via physical trapping methods like coagulation, membrane-based filtration and adsorption on specific adsorbents. The strategies based on simple physical separation cannot permanently address the pollution of MPs due to the lack of treatments to eliminate or recycle the separated and collected MPs debris and particles. This evidence has led to the development of chemical strategies to degrade and permanently remove MPs. The most recently investigated methods for the treatment of microplastics are Advanced Oxidation Processes (AOPs) and biodegradation [20–23]. AOPs include various degradation strategies able to eliminate organic pollutants by Reactive Oxygen Species (ROS), such as $OH^{\bullet}$ and $O_2^{\bullet-}$, possessing high standard reduction potentials, which can non-selectively break the chemical bonds allowing to degrade and even mineralize pollutants [24–33]. Biodegradation is driven by natural or modified enzymes and microorganisms, which are able to break down enzymatically the polymeric macromolecules into smaller fragments, potentially allowing the complete mineralization [34]. This process involves simple and easy operations and is characterized by low cost, flexibility, and relative safety. However, the biodegradation rates remain low and the impact of degradation products and the disposal of biomass resulting from biological treatment are still to be clarified [35, 36].

Besides efficient degradation processes, the scientific community and governments are looking for always more effective and easy scalable recycling methodologies [37–39]. Among the most used recycling strategies for plastics, chemical recycling is gaining importance, as it allows, at specific conditions, the recovery of the polymer matrix or the depolymerization of the waste to original monomers, fuels, or valuable low molecular weight chemicals (LMWCs) with potential for upcycled applications [40,41]. For example, LMWCs may be exploited as raw materials for the production of hydrogen or other chemical conversions. However, chemical recycling is still very expensive and energy-intensive compared to mechanical recycling and incineration. Similarly to solvent-assisted depolymerization processes, the catalytic oxidative degradation of microplastics may be used to obtain LMWCs without any involvement of strong acid or basic solutions, as well as supercritical solvents [42]. Catalytic oxidative degradation processes may be a valuable alternative for selectively converting plastic wastes to valuable and isolable chemicals.

Recently, an innovative strategy of pollutants degradation was proposed in which ROS were generated on the surface of inorganic-organic hybrid gel-derived materials at room temperature under indirect daylight without requiring any excitation source [43,44]. It was shown that this behavior was driven by the formation of Ligand-to-Metal Charge Transfer (LMCT) complexes occurring between suitable organic molecules and titanium or zirconium [45–47].

In this work, a new hybrid TiO_2-based material was synthesized, by a waste-to-wealth approach, adopting a sol-gel route that makes use of green solvents, available materials, and energy-efficient protocols. The organic constituent is rosin, a bio-waste material, composed by a mixture of resin acids and natural terpenes derived from the distillation of pine resin, from tall oil (a by-product of the Kraft process) or from aged pine stumps. Rosin often requires costly and time-consuming chemical transformations to be used in the synthesis of new materials. Here its direct conjugation with titanium was obtained by a simple sol-gel procedure. The obtained organic-modified TiO_2 material, "T-*Abi*", was able to promote the oxidative degradation at room temperature of polymeric films of linear low-density polyethylene (LLDPE) under indirect daylight conditions. In these mild conditions, a remarkable oxidative degradation of LLDPE films was observed within 1 month producing alkanes, alcohols, esters as degradation by-products. This stands out to be a promising process to degrade plastic wastes for two main reasons: no secondary pollutants are formed, and the degradation by-products detected by GC-MS are the proof that this process can be optimized to become in the future an example of tertiary recycling [21]. The wide structural and physico-chemical characterization, supported also by density functional theory (DFT) calculations, has revealed that the bio-waste modified TiO_2 material allows the stabilization of radical anions ($O_2^{\bullet-}$) on its surface, playing a key role in the oxidative degradation mechanism of LLDPE.

2. Experimental

2.1. Materials

All chemicals were used as received without further purification. Titanium (IV) *n*-butoxide (Ti(OBu)$_4$, 97+ %) and ethanol (EtOH, 99.8+ %) were provided by Sigma-Aldrich (Milan, Italy). Commercial rosin was used as bio-waste. Flexirene FG 20 F, a linear low-density polyethylene (LLDPE), manufactured as 150 μm thick films, was supplied by Blu Plast s.r.l.

2.2. Synthesis of T-Abi hybrid material

The hybrid TiO$_2$-based material was prepared by a hydrolytic sol-gel route. In a typical procedure, a solution containing 5 mL of titanium (IV) *n*-butoxide, 20 mL of ethanol and 0.88 g of rosin (acting as a complexing ligand) was prepared and stirred for about 30 min. Then a second solution containing distilled water and ethanol was prepared and mixed with the first one. The resulting molar ratio Ti: rosin: ethanol: water was 1: 0.2: 24: 4. The final solution was stirred for 2 h and after ageing at room temperature for 24 h, it was centrifuged. The resulting particulate gel was dried at 50 °C in a ventilated oven until constant weight to obtain a light-yellow powder material, named T-*Abi* as abietic acid was the major component of the rosin.

2.3. Computational details

DFT calculations were performed within Periodic Boundary Conditions (PBC) using the Perdew-Burke-Ernzerhof (PBE) exchange-correlation functional based on the generalized gradient approximation (GGA) [48] and ultrasoft pseudopotentials. The spin polarized Kohn-Sham equations were solved in the plane wave pseudopotential framework, with the wavefunction basis set and the Fourier representation of the charge density being limited by kinetic cutoffs of 25 and 250 Ry, respectively. The Quantum Expresso code [49] was employed for all calculations. It is well established that the addition of a Hubbard U term acting on the Ti 3d orbitals allows for a more accurate description of the electronic structure of titanium dioxide-based materials [50, 51]. In line with previous studies, we employed a U value of 3.9 eV [45, 52,53].

The abietic acid (HAbi) molecule interacts with the TiO$_2$ anatase surface (ATiO$_2$) in its deprotonated form (abietate, Abi), therefore all simulations were carried out in neutral conditions adding a proton H$^+$ as counter-ion on O2c (bi-coordinated O) atoms of the bottom layer of the surface according to previous theoretical studies [45,54,55].

Periodic slabs of ATiO$_2$ (101) were modeled by using a tetragonal (3 × 3) supercell with (TiO$_2$)$_{54}$ units and three TiO$_2$ layers, for a total of 162 atoms, with a vacuum separation of 30 Å. The Brillouin zone integration was performed on the Γ point only.

The O-defective system (161 atoms) was modeled by removing an O2c atom from the external layer of the metal-oxide surface (VO1) having the lowest formation energies (E$_{form}$) [45]. The modeled system consists of 214(213) atoms when the abietate adsorption occurs on stoichiometric (O-defective) TiO$_2$ (101).

The adsorption energy of abietate was computed using the formula E$_{ads}$= E$_{SURF/Abi}$ - (E$_{SURF}$ + E$_{HAbi}$), where E$_{SURF/Abi}$ is the energy of the combined system (namely the surface plus the abietate), E$_{SURF}$ is the energy of the stoichiometric (E$_{ATiO2\ (101)}$) and/or O-defective surface (E$_{VO1}$) alone, and E$_{HAbi}$ is the energy of the abietic acid in gas phase. Oxygen molecules adsorption was calculated by using E$_{ads}$(O$_2$) = E$_{SURF/Abi/nO2}$ - (E$_{SURF/Abi}$ + nE$_{O2}$) where E$_{SURF/Abi/nO2}$ is the energy of the system in which the oxygen molecules are adsorbed on the anatase surface in presence of organic ligand and nE$_{O2}$ is the energy of the oxygen molecule in gas phase.

Electronic properties were investigated only for the most stable O-defective anatase (101) surface (VO1) with which the organic ligand interacts more strongly than stoichiometric ATiO$_2$ (101) one.

The charge analysis was performed following the Bader's theory since the charge enclosed within the Bader volume can be considered a good approximation of the total electronic charge of an atom [56,57]. The differences between the Bader charges of the gas phase and coordinated abietate and O$_2$ molecules (Δq, e$^-$) were calculated according to the equation Δq = Σ q(SURF/Abi *or* SURF/Abi/nO$_2$) - Σ q(HAbi *or* nO$_2$), where Σ q(SURF/Abi *or* SURF/Abi/nO$_2$) is the sum of the Bader charges of abietate and nO$_2$ in presence of organic ligand adsorbed on VO1 anatase surface, while Σ q(HAbi *or* nO$_2$) is the sum of the free abietate and nO$_2$.

Benchmark calculations were performed to understand the role of van der Waals (vdW) interactions on the adsorption of abietate on the ATiO$_2$ (101) surface, employing the zero damping DFT-D3 method of Grimme [58]. Since the corresponding results suggested that the inclusion of vdW forces does not change the energy stability trend, the E$_{ads}$ deriving from the vdW calculations will not be considered in this work.

2.4. Physicochemical characterization of T-Abi

The chemical structure of the chosen bio-waste and that of the synthesized T-*Abi* were studied by Fourier Transform Infrared (FTIR) spectroscopy by using a Nicolet Instrument Nexus model (Thermo Scientific, Waltham, MA, USA) that was equipped with a DTGS KBr (deuterated triglycine sulfate with potassium bromide windows) detector. FTIR spectra were recorded in the 4000–400 cm^{-1} range at a resolution of 2 cm^{-1} on pressed disks of powders that had been previously diluted in KBr (1 wt%). The FTIR spectrum of each sample was corrected based on a spectrum of blank KBr.

X-Ray Diffraction (XRD) experiments were carried out with a Malvern Panalytical diffractometer (Malvern, UK) with a nickel filter and Cu Kα radiation to investigate the structure of the rosin sample and T-*Abi*.

Following the X-ray Photoelectron Spectroscopy (XPS), it was possible to assess that the rosin samples are mainly abietic acid in agreement with the speciation and the composition (at%). XPS analyses were performed on powdered samples mounted on copper bi-adhesive tape and analyzed by a Theta Probe spectrometer (Thermo Fisher Scientific) equipped with an Al Kα X-ray source (h*ν* = 1486.6 eV). A nominal 400 μm spot size (100.5 W) was used for acquiring the spectra. Survey and high-resolution spectra were obtained in fixed analyzer transmission (FAT) mode and the pass energy was set at 200 eV and 100 eV for the wide scan and narrow (high resolution spectra) scan spectra, respectively. Under these conditions, the full width at half-maximum of Ag 3d$_{5/2}$ peak acquired on a sputtered silver sample was 0.96 eV. To verify the linearity of the binding energy scale, a periodic calibration was performed following ISO 15472:2010. A flood gun neutralizer was used to compensate for sample charging. The spectra were acquired in the standard lens mode, and, under this condition, the emission angle was 53°. For each sample, three different areas were analyzed. The total duration of the acquisition was 30 min in each analyzed area. The binding energy scale was referenced to the aliphatic carbon component at 285.0 eV.

XPS spectra were processed by CasaXPS software (version 2.3.24PR1.0) [59]. An iterated Shirley – Sherwood background was subtracted before curve fitting. The product of Gaussian and Lorentzian functions was used as model functions. Quantitative composition was calculated using the first-principle method [60] under the assumption that the samples were homogeneous in composition.

The optical properties of T-*Abi* were investigated by performing Diffuse-Reflectance UV–vis (DRUV) measurements with a UV-2600i UV–VIS spectrophotometer, 230 V (Shimadzu, Milan, Italy), equipped with an integrating sphere ISR-2600Plus operating in a wavelength range of 220–1400 nm. Barium sulfate was used as a reflectance standard. The measured intensity was expressed as the value of the Kubelka-Munk function, F(R), while the direct band-gap energy value was evaluated according to the Tauc-plot linearization of (F(R)h*ν*)$^{1/2}$ against h*ν*.

Electron Paramagnetic Resonance (EPR) spectroscopy was exploited to check the presence of radical species on the studied material. The spectra were acquired at room temperature with an X-band (9 GHz) Bruker Elexys E-500 spectrometer (Bruker, Rheinstetten, Germany), collecting 16 scans, selecting the following instrumental settings: sweep width, 140 G; resolution, 1024 points; modulation frequency, 100 kHz; modulation amplitude, 1.0 G; time constant, 20.5 ms; attenuation, 10 dB. The g-factor values were evaluated by means of an internal standard, Mn^{2+}-doped MgO. An EPR spin-trapping experiment was also performed to detect ROS generation in aqueous environment. The following procedure was adopted: a specific amount of 5,5-dimethyl-1-pyrroline-1-oxide (DMPO) spin-trap (20 mmol/L) was added to an aqueous suspension of T-*Abi* at a concentration of 1 mg/mL kept in dark. After 10 min from the dispersion preparation, the sample was centrifuged to recover the supernatant, which was placed in a capillary to be analyzed by EPR. The spectrum was recorded with an attenuation of 15 dB and 64 scans were accumulated.

The Thermogravimetric (TG) and Differential Thermal (DTA) analyses were conducted to investigate the thermal behavior of T-*Abi* by using a TA Instrument simultaneous thermo-analyzer SDT Q600 (TA instrument, New Castle, DE, USA). To evaluate the weight loss, about 10 mg of the sample was placed in a platinum pan and tested in inert atmosphere. The analysis was carried out in the temperature range between 25 °C and 900 °C with a heating rate of 10 °C/min.

2.5. LLDPE degradation tests

A reaction system was set-up as follows. An aqueous suspension of T-*Abi* (1 mg/mL) was prepared in a 50 mL volume becker. Then, after stirring it for about 10 min, 12 pieces of LLDPE films (5 mm × 5 mm) were added to the suspension. The whole system was kept under magnetic stirring for 4 days, 14 days and 1 month, so to investigate the degradation of the polymeric films at different incubation times. The tests were performed at room temperature (about 30 °C) in indirect daylight conditions, i.e., under artificial laboratory illumination during the working days and darkness along the night. The analysis of the treated LLDPE samples was carried out in triplicate at each time point.

2.6. Characterization of LLDPE films

XRD analysis on polymeric films was performed as previously described to check the change in the crystalline structure of LLDPE following the treatment with T-*Abi*. The crystal structure of polyethylene is orthorhombic and for the orthorhombic system the values of a and b can be calculated with the equation:

$$\frac{1}{d^2} = \frac{h^2}{a^2} + \frac{k^2}{b^2} + \frac{l^2}{c^2} \tag{1}$$

Where d is defined as the distance between adjacent planes in the set (hkl), while the crystallinity index (X_c) is a quantitative indicator of crystallinity, and it was calculated according to:

$$\text{Crystallinity } index, \ X_c(\%) = \frac{\text{Area of all the crystalline } peaks}{\text{Area of all the crystalline and amorphous } peaks} \tag{2}$$

In addition, the mean crystallite sizes were determined taking advantage of Scherrer's equation:

$$D = \frac{k\lambda}{\beta \cos\theta} \tag{3}$$

Where D is the mean size of the crystallite domains, k is a dimensionless shape factor generally considered as 0.9, λ is the X-ray wavelength, β is the half-height width (FWHM) and θ is the Bragg angle.

Thermal properties of LLDPE samples were determined by performing a Differential Scanning Calorimetry (DSC) analysis. DSC mea-

surements were carried out on film samples by using the same TA instrument described above for TG-DTA. The melting enthalpy was determined by integrating the melting peak using the software Origin-Pro by OriginLab Corporation. The degree of crystallization of the samples was calculated by dividing ΔH_m (i.e., the sample melting enthalpy), by ΔH_0 (i.e., the theoretical value of the melting enthalpy of 100 % crystalline LDPE):

$$\text{Crystallinity } index, \ X_c(\%) = \frac{\Delta H_m}{\Delta H_0}(\%) \tag{4}$$

The value $\Delta H_0 = 293$ J/g was used in calculations [61].

Attenuated Total Reflectance Fourier Transform Infrared spectroscopy (ATR-FTIR) analysis on LLDPE films was carried out for finding out any alterations in the chemical structure. The samples were placed on a ZnSe crystal, and the ATR-FTIR absorption spectra were recorded in the 4000–400 cm^{-1} range with 8 cm^{-1} spectral resolution. The spectrum of each sample was corrected for that of blank, which was carried out in air. ATR-FTIR spectra allowed the estimation of the degradation efficiency of LLDPE films through the Carbonyl Index (C.I.) method [62]. C. I. was calculated as the ratio between the absorbance of the carbonyl groups (1700–1500 cm^{-1}) and the absorbance of the reference peak of CH_2 and CH_3 at (1480–1420 cm^{-1}) [63]:

$$\text{Carbonyl } Index \ (C.I.) = \frac{\text{Absorption of carbonyl } species \ (1700 - 1500cm^{-1})}{\text{Absorption } of \ CH_2, \ CH_3 \ (1480 - 1420cm^{-1})} \tag{5}$$

2.7. Identification of degradation by-products from LLDPE by GC-MS

The degradation intermediates were identified by Gas Chromatography-Mass Spectrometry (GC-MS) according to the standard spectra of the NIST 1.7 library data. Prior to GC-MS analysis, the lyophilized samples, obtained after 1 month of incubation of LLDPE with T-*Abi*, were extracted by using three different organic solvents, toluene, hexane and chloroform. The same experimental procedure was performed for the controls, obtained after the same incubation time (1 month) but without T-*Abi*.

All the samples were analysed on a Perkin Elmer AutoSystemTMXL GC, equipped with a Programmed Temperature Split/Splitless injector; a Restek Rtx-5MS capillary column (5 % diphenyl-95 % dimethylpolysiloxane, 30 m × 0.25 mm, 0.25 μm) and a Perkin-Elmer Turbo Mass Goldmass-spectrometer. The initial temperature of the column oven was held at 40 °C for 5 min, and then heated up to 285 °C at a ramping rate of 5 °C/min. Helium was used as carrier gas. Mass spectrometric detection was operated with 70 eV electron impact (EI) mode at an ionization current of 50 μA and an ion source temperature of 250 °C. The mass spectra were recorded in a full scan mode (m/z 50–1000) for qualitative analysis.

3. Results and discussion

3.1. Bio-waste characterization

Rosin, a natural bio-waste generally consisting in a mixture of resin acids, was chosen to explore its interaction with titanium, based on the coordination ability of carboxylic acids, and the potential consequences on the redox properties of the modified titanium oxide. An accurate chemical characterization of the bio-waste was first carried out by XRD, XPS and FTIR analyses. The XRD pattern shows the broad peak at about 15° of 2θ typical of rosins [64] (Fig. S1). XPS survey spectra acquired on a powdered bio-waste sample indicate the presence of only carbon and oxygen (Fig. 1a). The curve fitting of high-resolution spectra of C 1s (Fig. 1b) and O 1s (Fig. 1c) signals was performed considering the functional groups and the stoichiometry of abietic acid, assuming that this compound is the major component of the bio-waste sample. In order to take into account the presence of abietic acid, C 1 s signal (Fig. 1b)
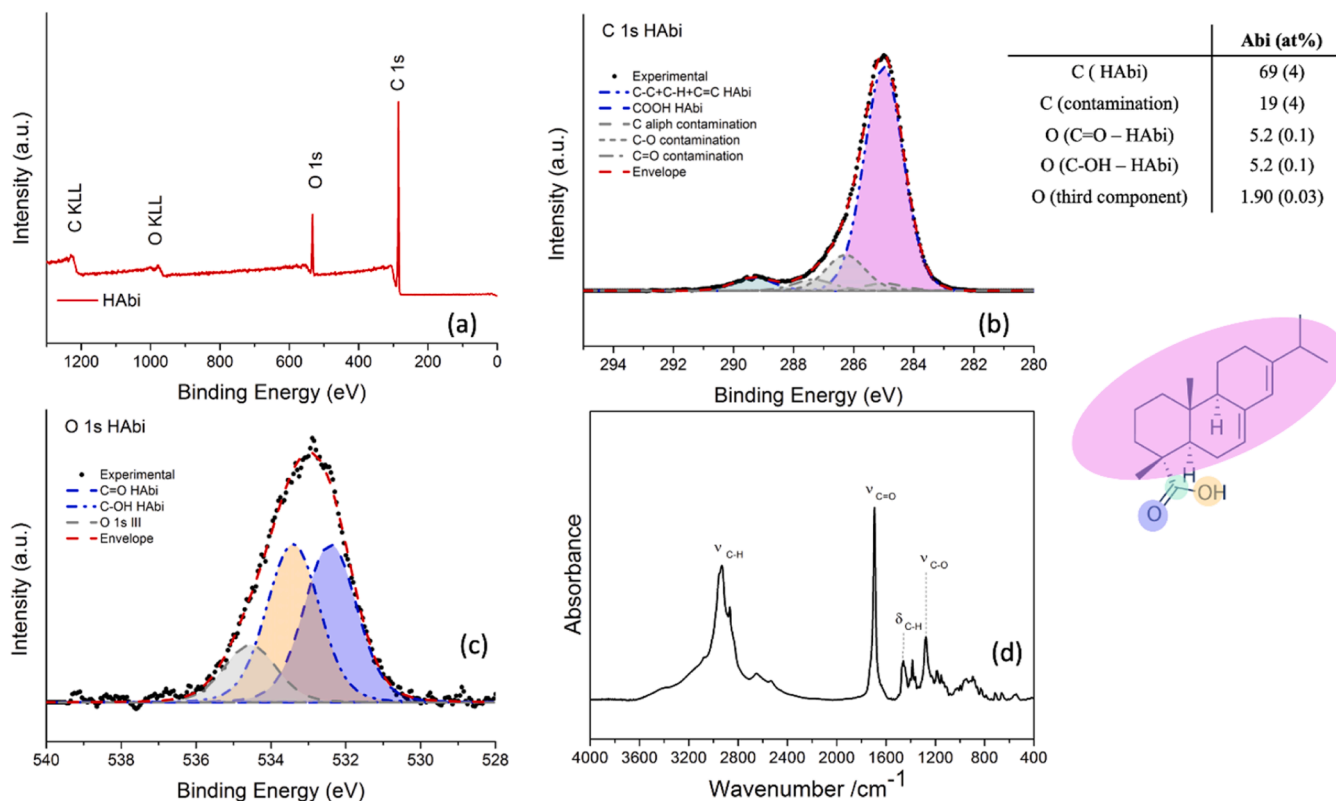
Fig. 1. XPS spectra of the powdered bio-waste sample: a) survey spectrum; b) C 1 s high-resolution spectrum: aliphatic and olefinic carbons are shadowed in pink (BE = 285.0 eV), carboxylic carbon in green (BE = 289.3 eV), c) O 1 s high-resolution spectrum: C═O oxygen of carboxylic group (BE = 532.4 eV) is shadowed in blue and C-OH oxygen (BE = 533.4 eV) in orange; d) FTIR spectrum of the bio-waste. The structure of abietic acid and the quantitative composition (at%) by XPS analysis are also reported.

was fitted considering two components ascribed to aliphatic and olefinic carbon and to carboxylic carbon of the abietic acid, located at 285.0 (0.1) eV and 289.3 (0.2) eV [65] respectively and with an area ratio of 17:1 according to the stoichiometry of the chemical formula provided in Fig. 1. Three components, which are not assignable to abietic acid, might be attributed to aliphatic carbon (BE = 285.0 eV), and to other organic compounds with functional groups as C-O (BE = 286.3 (0.2) eV) and C═O (287.5 (0.2) eV) [65]. These species may be present in the mixture but the possible contribution of organic contamination due to contact of the samples with the environment cannot be ruled out. These components are shadowed in gray in Fig. 1b.

The O 1 s signal was fitted with two Gaussian/Lorentzian curves at 532.4 (0.1) eV and 533.4 (0.1) eV ascribed to C═O and to C-OH oxygen in carboxylic group, respectively [66]. The area ratio between these components is constrained equal to 1, according to the stoichiometry. A further component is found at 534.6 eV and it might be ascribed to adsorbed oxygen-containing compounds [67]. Another possibility for the presence such a component might be the Auger signal of sodium, but sodium contamination can be ruled out since other Na signals are not revealed.

The quantitative composition of the powdered bio-waste sample is given in the Table reported in Fig. 1. Considering C1s signal, it is possible to estimate the amount of abietic acid in the bio-waste and it resulted to be about 80 %. The experimental $(O_{C═O - Abi} + O_{C-OH - Abi})/C_{Abi}$ at% ratio was found to be 0.15 (0.01), that is higher than the expected ratio from stoichiometry (0.11). This might be due to the presence of other carboxylate-bearing constituents of the bio-waste.

The chemical structure of the bio-waste was further investigated by FTIR spectroscopy. The material exhibits absorption bands at 2958 cm^{-1} and 2934 cm^{-1} ($\nu_{as\ C-H}$), at 2868 cm^{-1} ($\nu_{s\ C-H}$) and a pronounced one at 1693 cm^{-1} ($\nu_{C═O}$) (Fig. 2). Absorption bands at 1460 cm^{-1} ($\delta_{as\ C-H}$) and

at 1278 cm^{-1} (ν_{C-O}) are also observed. The assignment of recognized IR bands (Fig. S2) is summarized in Table S1.

Therefore, according to the above results, it can be asserted that the adopted bio-waste is mainly constituted by abietic acid, the major terpene belonging to the mixture of resin acids [68–70].

In the following, the bio-waste at issue will be considered as formed by abietic acid only and will be indicated as HAbi.

3.2. Theoretical investigation of the interaction between abietic acid and TiO$_2$ surface

Once known the chemical composition of the bio-waste, before designing a synthesis procedure, DFT calculations were employed to verify if the abietic acid can form LMCT complexes with Ti^{4+}, as occurred for carboxylic acids, diols, β-diketones [45]. These complexes play a key role in the stabilization of ROS species on the surface of the hybrid materials [43–45]. To this aim, a detailed study of the interaction between abietic acid molecule and stoichiometric as well as O-defective TiO$_2$ anatase (101) surfaces (Fig. S3 of the SI) was performed. As a matter of fact, due to its disordered structure, the anatase surface with oxygen vacancies may better represent the hybrid surface than a stoichiometric one. Reduced TiO$_2$ (101) anatase surface was modeled by removing a two-coordinated O atom from the external layer of the surface resulting in two unsaturated and reduced Ti^{3+} atoms. This O vacancy is the most favorable showing the lowest O vacancy formation energy, in agreement with previous studies [45,71].

The abietic acid molecule is expected to interact with TiO$_2$ in its deprotonated form (abietate, Abi). The adsorption energies (E$_{ads}$, eV) of the most stable interaction between abietate and stoichiometric TiO$_2$ anatase surface, ATiO$_2$ (101) surface, is − 1.4 eV (see SI, Fig. S3). Despite this quite favorable E$_{ads}$ value, our results indicate that the
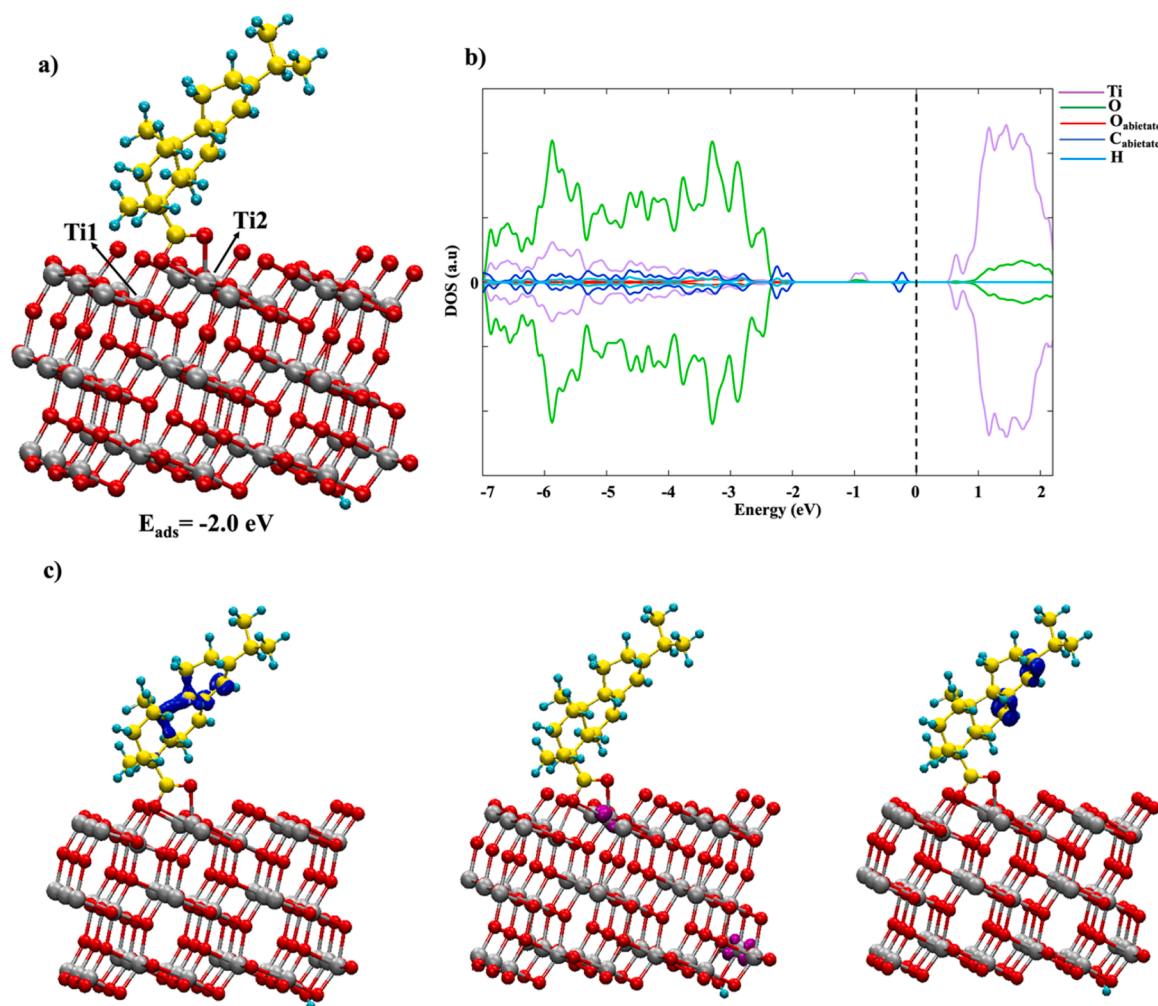
Fig. 2. a) Optimized structure of the interaction of abietate with O-defective anatase surface (101) with the corresponding E_{ads} (eV). Ti, C, H, and O surface and ligand atoms are represented in ball and sticks and depicted in gray, yellow, cyan, and red, respectively. b) PDOS and c) spin density plots for abietate on VO1 system, respectively. The state of titanium (Ti) and oxygen (O) surface atoms, oxygen (O_{ab}), carbon (C) and hydrogen (H) ligand atoms are represented in purple, green, red, blue, and cyan, respectively. On the DOS (a.u.) axis, the values above and below 0 a.u. indicate the electrons with spin up and spin down, respectively. The Fermi energy level is represented with a red line at 0 eV.

adsorption of the organic ligand on O-defective anatase surface (VO1) remains preferred by 0.6 eV. For this reason, in the following, we will focus only on the interaction between the abietate and the reduced anatase surface (101).

3.2.1. Adsorption of abietate on the O-defective anatase (101) surface

Fig. 2a shows the optimized geometry of the most stable structure with the abietate adsorbed on the reduced anatase surface VO1. The computed value of the adsorption energy is of − 2.0 eV. In this configuration the abietate molecule coordinates the VO1 surface adopting a bidentate coordination mode with the oxygen atoms of the carboxylate group bonded to the two tetra-coordinated reduced Ti^{3+} atoms (Ti1 and Ti2) deriving from the formation of the vacancy VO1. As a result, abietate restores the hexa-coordinated configuration of Ti1 and Ti2.

The PDOS plots of the lowest energy configuration of abietate co-ordinated to VO1 surface, displayed in Fig. 2b, show a valence band (VB) with mainly O 2s and 2p characters and a conduction band (CB) with Ti 3d character. The computed value of the bandgap is 2.3 eV, in agreement with the experimentally calculated value (see below). This value is smaller than the one calculated for other carboxylic acids [46], and β-diketones [45] as well as for the stoichiometric anatase surface (experimental gap of 3.2 eV [53,72,73] and theoretical gap of 3.0 eV [45,53]), suggesting that the coordination of abietate significantly

reduces the TiO_2 surface bandgap. Filled bandgap states are generated due to the conjugated double bond of the diterpene (blue peaks between −2.0 and −2.2 eV and at −0.2 eV) and the two reduced Ti^{3+} atoms (purple peaks at −0.9 eV) [45] as confirmed by spin density analyses where the electron excess on the organic ligand and the two Ti^{3+} are indicated with blue and purple densities, respectively, analogously to the colors of the respective bandgap peaks (Fig. 2c).

The computed variation of Bader charges (Δq, e⁻), calculated as the difference between the charges of the ligand atoms in VO1-bound and free forms, indicates a charge transfer from the organic ligand to VO1 of about 0.3 e⁻ which adds to the excess charge already present on the surface, in agreement with the LMCT suggested by DRUV spectroscopy.

3.2.2. Adsorption of O_2 molecules on the O-defective anatase (101) surface coordinated with abietate

In order to investigate the capability of the abietate-modified TiO_2 to form ROS in ambient conditions, the interaction between O_2 molecules and the hybrid surface was simulated. Fig. 3a shows a plot of two O_2 molecules (representative of the "high oxygen coverage" which better reproduces the experimental conditions [45]) adsorbed on the O-defective anatase (101) surface VO1 in presence of the coordinated organic ligand. In this case, the two O_2 molecules bind VO1 with an adsorption energy of − 1.2 eV.
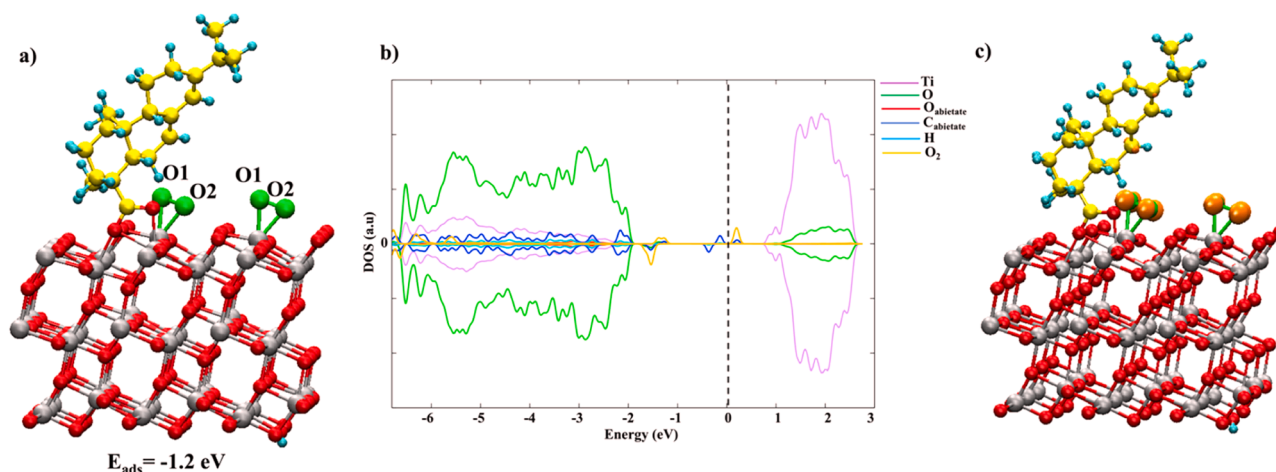
Fig. 3. a) Optimized structure of two O_2 adsorption on VO1 surface in presence of abietate with the corresponding E_{ads} (eV). Ti, C, H, O surface and ligand atoms and O_2 molecules are represented in ball and sticks and depicted in gray, yellow, cyan, red, and green respectively. b) PDOS and c) spin density plots for 2 O_2 on O-defective anatase (101) surface in presence of abietate, respectively. The state of titanium (Ti) and oxygen (O) surface atoms, oxygen (O_{ab}), carbon (C), hydrogen (H) ligand atoms and oxygen (O_2) molecules are represented in purple, green, red, blue, cyan and orange, respectively. On the DOS (a.u.) axis, the values above and below 0 a.u. indicate the electrons with spin up and spin down, respectively. The Fermi energy level is represented with a red line at 0 eV.

The adsorption of the O_2 molecules on VO1 is accompanied by a charge transfer from the surface to the O_2 molecules that turn into superoxide radical anions ($O_2^{\bullet-}$). The superoxide radical anions formation is confirmed by the O-O bond elongation, which goes from 1.23 Å in the gas phase O_2 molecule to 1.33 Å in the surface-bound form, and by the change in the magnetic moment (μ) for each oxygen atom ($|\mu O1| \, |\mu O2|$), which becomes half of the original magnetic moment of O_2 in gas phase ($|0.5| \, |0.5|$ vs $|1.0| \, |1.0|$). This is confirmed by the Bader charge analysis (Δq, e^-) that indicates a gain of 0.5e^- for each oxygen atom in the O_2

adsorbed form compared to the O_2 free form and by spin density analyses in Fig. 3 [45,74,75]. In addition, the PDOS plot (Fig. 3b) reveals that the adsorption of two O_2 molecules (high oxygen coverage) generates band gap states related to the transfer of the two electrons from the surface to the π^* orbital of each oxygen molecule (orange peak), while the bandgap states related to Ti^{3+} disappear (see purple peaks in Fig. 2b), indicating that the formation of two $O_2^{\bullet-}$ is accompanied by oxidation of Ti^{3+} to Ti^{4+} [47,76,77]. PDOS plot also displays a bandgap state above the Fermi level (0 eV) corresponding to the empty
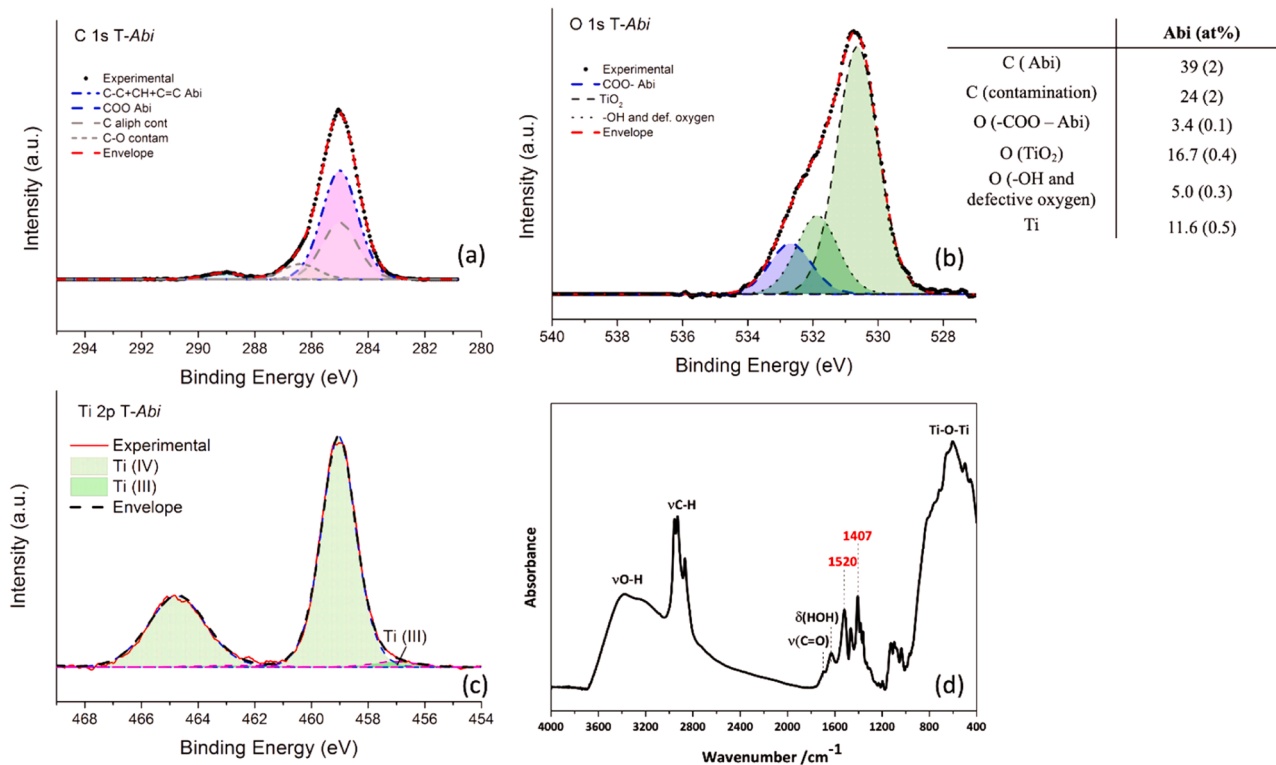

Fig. 4. XPS spectra of the T-*Abi* sample: a) C 1 s high-resolution spectrum: aliphatic and olefinic carbons are shadowed in pink (BE = 285.0 eV), carboxylic carbon in green (BE = 289.3 eV), b) O 1 s high-resolution spectrum: the components ascribed to O^{2-} (BE = 530.7 eV) and OH^- (BE = 531.9 eV) or oxygen in defective sites are shadowed in green; COO^- oxygen atoms of carboxylic group from the abietic acid (BE = 532.7 eV) is shadowed in blue; c) Ti 2p signal; d) FTIR spectrum of T-*Abi*. The quantitative composition (at%) by XPS analysis is reported in the Table.

σ2p* orbital of the O_2 molecules. This is further evidence that the O_2 high coverage adsorption leads to the formation of superoxide radical anions $O_2^{\bullet-}$.

The PDOS plots in the absence and in the presence of O_2 (compare Figs. 2b and 3b) confirm that the adsorption of oxygen molecules does not affect the bandgap value of the system, which remains unchanged at 2.3 eV.

3.3. Physicochemical characterization of T-Abi hybrid material

Following the encouraging results of DFT modeling, a TiO_2-abietate (T-*Abi*) hybrid material was synthesized via sol-gel and its chemical, structural, and optoelectronic properties were characterized in detail.

XPS survey of T-*Abi* shows the presence of Ti signals together with carbon and oxygen ones (Fig. S4). The high-resolution spectra of C 1s, O 1s and Ti 2p and the quantitative composition (at%) of the hybrid material determined by XPS are given in the Table reported in Fig. 4. Curve fitting was performed for substantiating and implementing the information on the charge transfer complex T-*Abi*. Curve fitting was performed using the same parameters applied for verifying the composition of the Abi sample. The carbon C1s signal was fitted with two components ascribed to the aliphatic and olefinic carbon and to the carboxylic carbon of the abietic acid; the signals were found at 285.0 (0.1) eV and 289.3 (0.2) eV [65] (Fig. 4a). Also, in this case two more components are found (Fig. 4a). They do not belong to the abietic acid and they might be assigned to aliphatic (BE = 285.0 eV) and to C-O (BE = 286.3 (0.2) eV) bearing-functional groups [65] from different species including alcohol molecules derived from the synthesis of the material and organic contamination due to contact with the environment.

The oxygen, O 1 s signal, was also multicomponent and it was fitted with three model curves: the one at binding energy of 530.7 (0.1) eV is ascribed to the oxygen atoms in TiO_2, -OH and oxygen in defective sites is detected at 531.9 (0.1) [72] and the peak at 532.7 (0.1) eV is assigned to the carboxylic group of the abietic acid coordinating Ti atoms. This finding is substantiating the hypothesis of the bidentate coordination mode of abietic acid (Fig. 4b).

As far as the titanium, the most intense photoelectron signal is the Ti 2p peak (Fig. 4c). It is characterized by the presence of an intense doublet due to the spin orbit splitting assigned to Ti (IV); a less intense doublet due to the presence of small amounts of Ti (III). The binding energy of the Ti $2p_{3/2}$ components of the two doublets was found to be 459.1 (0.1) eV and 457.2 (0.1) eV for Ti (IV) and Ti (III) respectively, in agreement with [72].

The quantitative composition in at% of the T-*Abi* sample determined by XPS was calculated assuming the homogeneity of the sample and it is presented in the Table reported in Fig. 4. The results show that titanium at the surface is only partially coordinated by Abi ligands, since according to the hypothesis of the bidentate coordination mode, the stoichiometric ratio between Ti and O_{Abi} should be 1:1, and the expected ratio between these two signals would be 2.5 considering the nominal molar composition of the sample (Abi/Ti = 0.2), while the experimental one is 3.4 (0.2). This difference is due to the contribution of titanium oxide and hydroxides to Ti 2p signal, that is confirmed also by the presence of the correspondent signals in O 1s (Fig. 4b).

The hybrid nature and the coordination bonding of the T-*Abi* was additionally verified through FTIR spectroscopy. The FTIR spectrum of hybrid T-*Abi* (Fig. 4d) shows absorption bands above 3000 cm^{-1} (ν_{O-H}), near 2900 cm^{-1} (ν_{C-H}), at 1637 cm^{-1} (δ_{HOH}) and the vibrations of Ti-O-Ti bonds below 800 cm^{-1}. The comparison between the FTIR spectrum of the net Abi with that of T-*Abi* (Fig. S5) shows that the band related to C=O bonds at 1693 cm^{-1} ($\nu_{C=O}$) is shifted towards low wavenumbers in the spectrum of the hybrid material, giving the asymmetric and symmetric stretching at 1520 cm^{-1} ($\nu_{as\ C=O}$) and at 1407 cm^{-1} ($\nu_{s\ C=O}$) and proving that the carboxylate groups are involved in coordinative bonds with Ti^{4+} (Fig. S6). The splitting between these bands, Δ, is equal to 113 cm^{-1}, confirming also the bidentate interaction between abietate

and Ti^{4+} (Δ value lies in the 50 −150 cm^{-1} range), in agreement with XPS results and DFT calculations [78]. The structure of the synthesized hybrid material is substantially amorphous, as ascertained by its XRD pattern (data not shown).

DRUV analysis was also performed to explore the optical behavior of the hybrid material. The DRUV spectrum of T-*Abi* is characterized by a broad peak centered at around 250 nm with a shoulder like tail in the
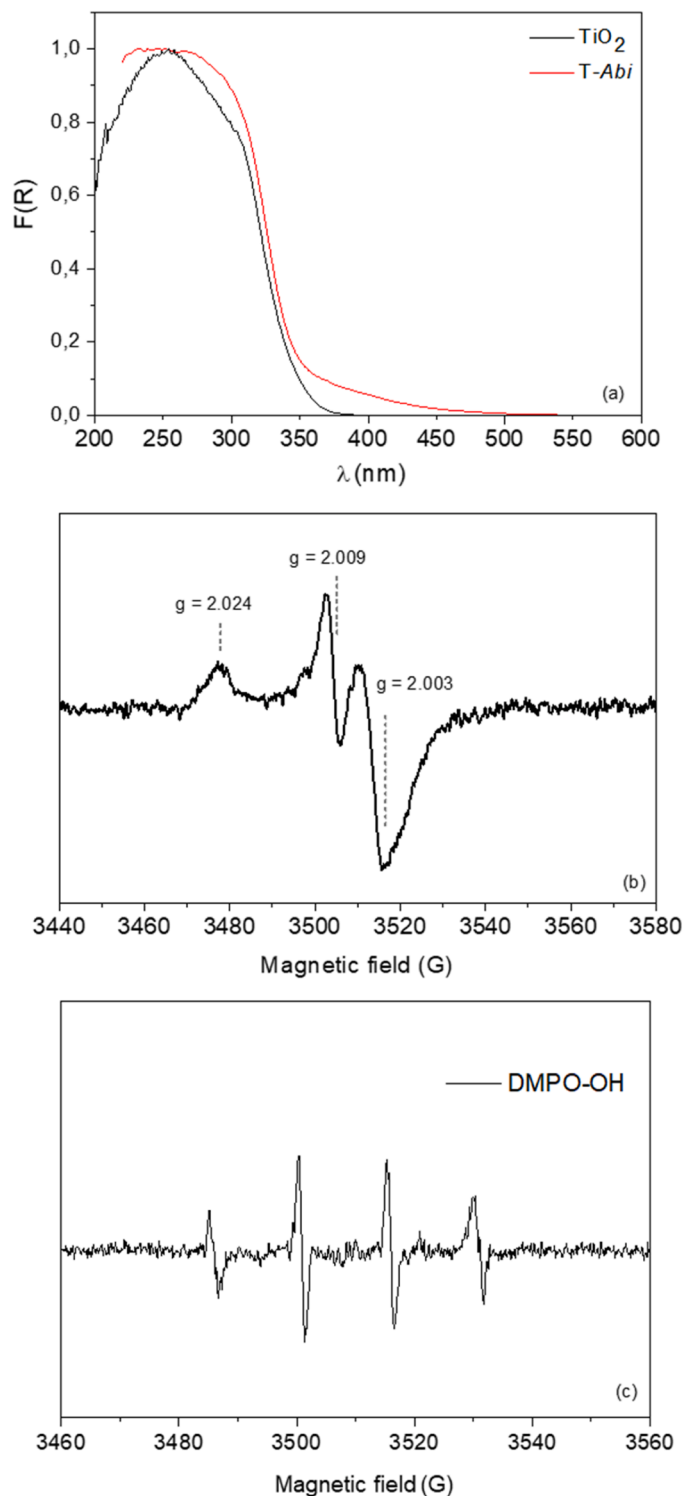

Fig. 5. DRUV spectra of bare TiO_2 and T-*Abi* (a); EPR spectra of T-*Abi* powder (b), and of DMPO-OH spin-adduct formed in aqueous medium in the presence of T-*Abi* (c).

visible region up to 500 nm, compared to a bare TiO_2 sample prepared by an analogous sol-gel procedure without the addition of HAbi (Fig. 5a). The implementation of Kubelka-Munk function and the Tauc plot linearization allowed the estimation of the effective band gap energy value, i.e., the energy gap resulting from the additional absorption band. It was estimated as shown in Fig. S7 [79], and results to be about 2.5 eV, in fair agreement with the value of 2.3 eV predicted by DFT (Section 3.2.1). The partial absorption in the visible region and the observed band gap are further evidence of the formation of a charge transfer complex of TiO_2 with the abietic acid ligand.

Moreover, the thermal stability of the hybrid T-*Abi* was investigated and the TG-DTA curves of T-*Abi* collected under N_2 atmosphere are reported in Fig. S8. The weight loss occurs in two main regions: below 200 °C and between 300 and 400 °C. The former (about 10 wt%), that takes place progressively from room temperature up to 200 °C, is related to the evacuation of water, solvent (ethanol) and the alkoxide molecules. The latter (about 46 wt%), that occurs fast, can be related to the volatilization of the organic ligands, as attested by the presence of two DTA endothermic peaks at about 319 and 356 °C in the corresponding DTA curve. This weight loss is close to the nominal mass content of HAbi in the hybrid material (43%).

The presence of superoxide radical ions on the surface of the hybrid TiO_2, suggested by the XPS data (presence of Ti(III) and defective oxygen) and predicted by DFT calculations (Section 3.2), was ascertained by EPR spectroscopy. Fig. 5b displays the EPR spectrum of the T-*Abi* xerogel powder, which was acquired at room temperature in the dark without any sample pre-treatment. The three-component signal shows the characteristic line shape and g values of the $O_2^{\bullet-}$ radical adsorbed on the surface of titanium oxide [74]. This result unambiguously proves that T-*Abi*, simply exposed to air in ambient conditions, generates $O_2^{\bullet-}$ radicals and maintains them stably adsorbed on its surface. This special ability was previously shown by TiO_2 hybrids with β-diketones as organic ligands [44,45,80]. Here we demonstrate that a carboxylic acid, such as the abietic acid, coordinated with titanium in the amorphous oxide matrix, can confer the same capability. This behavior can be related to the LMCT character of the complex, through the mechanism elucidated by DFT modeling (see Section 3.2). The EPR spectrum seems to include a relatively weak overlapped peak with a g value between 2.003 and 2.009, which could be ascribed to a carbon-centered radical species, likely formed on the organic ligand. Similar signals with varying intensity have been observed for different cyclic and aromatic molecules bonded with titanium in hybrid gels [46]. The spontaneous production of ROS on the surface of the hybrid material without the need for direct light irradiation encouraged us to test T-*Abi* in the oxidative degradation of a model microplastic. In particular, the EPR spin trapping method was employed to investigate the capability of T-*Abi* to generate ROS in the aqueous environment (Fig. 5c). The short lifetime of ROS in solution makes their direct determination by EPR very tough. Therefore, DMPO spin-trap was used, as it can react with unstable oxygen-centered radicals, forming new longer-living radical adducts observable by EPR. The appearance of a signal in the EPR spectrum of the supernatant was observed, showing a characteristic quartet with a 1:2:2:1 intensity ratio, which corresponds to the DMPO-OH adduct formed from the trapping of hydroxyl radical, $OH^{\bullet}$, on DMPO [43,81]. The quantitative analysis of this spectrum was realized determining the hyperfine coupling constants for the nitroxide nitrogen and for the β-proton ($a_N = a_{\beta H} = 14.8 \pm 0.1$ G), in agreement with those reported in the literature [43,81], thus confirming the formation of $OH^{\bullet}$ radicals. As previously reported [82,83], their most probable source is from surface adsorbed $O_2^{\bullet-}$ that easily reacts with water forming hydroperoxyl radical ($HO_2^{\bullet}$), then H_2O_2 and finally $OH^{\bullet}$, which may take part in the degradation of LLDPE.

Furthermore, it should be noted that the formation of Ti-abietate complexes hinders the auto-oxidation phenomena generally occurring in the case of resin acids that, according with time and temperature, transform into more oxidized compounds, like dehydroabietic acid, 15-hydroxy-7-oxodehydroabietic acid and isopimaric acid [68,69].

3.4. Degradation of LLDPE in the presence of T-Abi hybrid material

The ability of T-*Abi* to generate superoxide radicals on its surface and hydroxyl radicals in water makes it suitable for many different applications. In this work, T-*Abi* was tested in the oxidative degradation of LLDPE plastic samples as described in the Experimental section. Briefly, LLDPE samples were immersed in an aqueous suspension of T-*Abi* (1 mg/mL) and stirred by the aid of a magnetic stirrer until 1 month at indirect daylight, without any external excitation source. This choice was adopted both to exploit an oxidative degradation pathway closer to real environmental conditions, fulfilling the day-night illumination cycle, and to establish a green and cost effective microplastic decontamination strategy. After incubation, the aqueous suspension of T-*Abi* was recovered by centrifugation at 10,000 rpm for 10 min. The supernatant obtained was filtered (0.45 μm), subjected to extraction, and finally analysed by means of GC-MS. The GC-MS analysis of the degradation by-products obtained from LLDPE incubated for 1 month allowed us to identify various short-chain compounds, listed in Table S2 and showed in Fig. 6a, where the total chromatogram of the degradation products is also reported. The identified compounds can be included in three classes: alkanes, alcohols and esters (Fig. 6b); moreover, their absence in the control, obtained by incubating T-*Abi* for 1 month without LLDPE, demonstrates that the degradation of LLDPE occurred effectively.

The degradation by-products detected by GC-MS are recognized as environmentally friendly low-molecular-weight organic compounds. In previous works, similar organic compounds were found as intermediates of microplastics degradation. These latter were demonstrated to be of low toxicity, even acting as the carbon source for algae growth [84,85].

Considering that T-*Abi* is an amorphous material with a high content of organic component, a significant photooxidation contribution can be excluded (see Fig. S1). Amorphous TiO_2 is widely reported to have a very low photocatalytic effect because its disordered structure hinders the transport of photogenerated electron-hole pairs and its defects act as potential recombination centers [86,87]. The activity of T-*Abi* is not apparently affected by UV irradiation, as confirmed by preliminary experimental results obtained exposing LLDPE films for 4 days to UVA (nominal power of 125 W). The comparison between ATR-FTIR spectra of indirect daylight and UVA exposed LLDPE films indicates that the extent of degradation is very similar (data not shown), and it is not affected by exposure to an external radiation source.

3.4.1. Degradation mechanism

Based on the GC-MS results reported above, the following degradation mechanism of LLDPE might be proposed (Scheme 1).

As shown in Scheme 1, a possible route, occurring in the aqueous suspension, may involve the homolytic scission of LLDPE polymer in the presence of an $OH^{\bullet}$ radical, generated in solution by T-*Abi*, as demonstrated by the spin-trapping EPR spectrum of DMPO-OH adduct (Fig. 5c), forming a generic alkyl radical ($R_1\bullet$). This radical may be terminated by reaction with another alkyl radical ($R_2\bullet$), probably generated by a similar mechanism, to provide an alkane (R_3H). Alternatively, $R_1\bullet$ radical may undergo termination by reaction with an $OH^{\bullet}$ radical, resulting in the production of an alcohol (R_1OH). Due to the presence of the ROS species in solution, a further oxidation of the alcohol (R_1OH) can occur giving a carboxylic acid (R_4COOH). In this reaction environment, in presence of the T-*Abi*, the carboxylic acid (R_4COOH) could react with an alcohol (R_5OH) to form an ester (R_4COOR_5) through an esterification reaction, possibly aided by the acidic character of the TiO_2 surface.

In the literature, the mechanism generally reported for the photo-initiated oxidative degradation of LLDPE (or polypropylene) is the following [88–91]. In the initiation step, the photogenerated hydroxyl radicals $OH^{\bullet}$ break the C-H bonds on the polymer backbone and generate polyethylene alkyl radicals ($-CH_2-CH\bullet-$)$_n$. During propagation, an alkyl radical reacts with oxygen to form a peroxyl radical
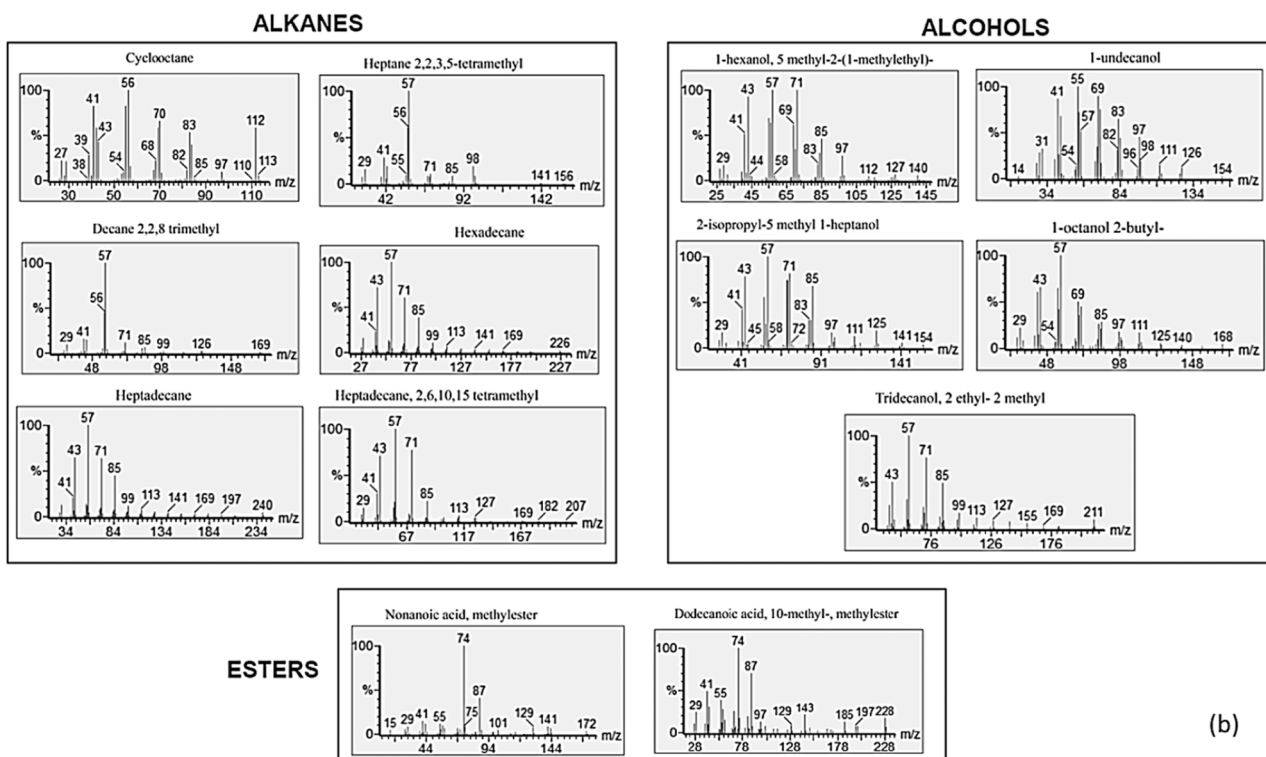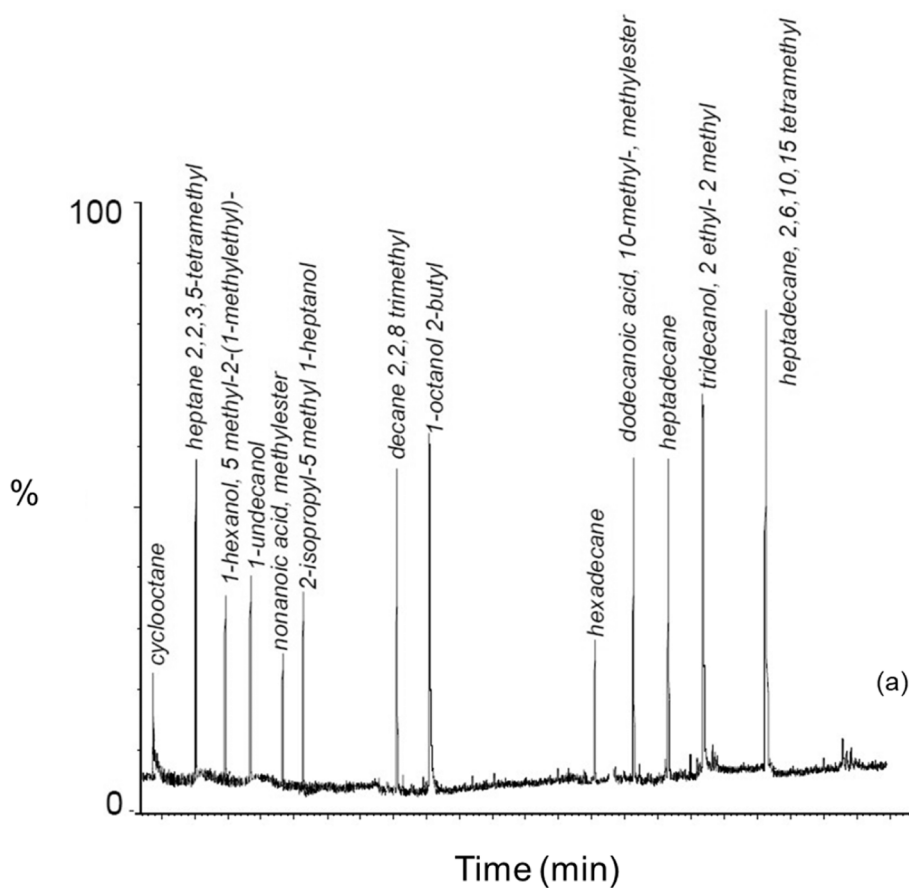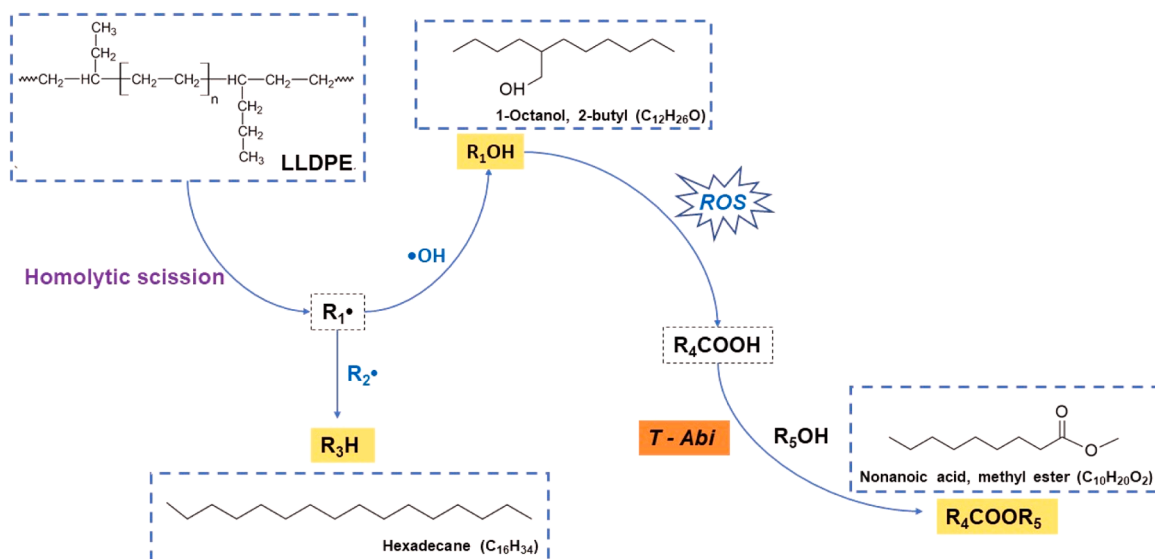
Fig. 6. Total chromatogram of the degradation by-products obtained after incubation of LLDPE with T-*Abi* for 1 month (a) and standard mass spectrum of each compound identified (b).

Scheme 1. Schematic representation of the possible LLDPE degradation mechanism in the presence of T-*Abi*.

($-CH_2-HCOO\bullet-CH_2-)_n$ that extracts a hydrogen atom from another polymer chain to form hydroperoxide species ($-CH_2-HCOOH-CH_2-)_n$. The hydroperoxide, an unstable specie, is further cleaved into two new free oxy and hydroxyl radicals by the scission of the weak O–O bond. In conclusion, β-scission and chain transfer of these carbon-centered radicals give rise to the random C–C backbone cleavage and molecular weight reduction. Accordingly, in the end, the existence of carbonyl compounds (e.g., aldehydes, carboxylic acids and ketones) usually confirms the photo-oxidative degradation of long- and short-branched polyolefins. Some similarities can be found between the above reported mechanism and the radical-mediated reaction pathway envisaged to occur in our case, driven by the generated ROS. As a matter of fact, both of them involve the formation of OH$^{\bullet}$ radicals that are either photogenerated or produced through the reaction of superoxide ion radicals with H_2O.

3.4.2. Characterization of LLDPE treated with T–Abi

The progressive modification and degradation of LLDPE was assessed after 4 days, 14 days and 1 month of processing (see Experimental) by means of XRD, DSC and ATR-FTIR.

Fig. 7a displays XRD diffractograms of bare LLDPE and the one treated for 1 month. XRD plot of bare LLDPE shows the typical reflections (i.e., (110), (200) and (020)) of the orthorhombic crystal structure, which are responsible for the appearance of three main peaks at 21.8°, 24.1° and 36.5° [92]. It is possible to observe that, in the case of treated LLDPE sample, these peaks shift to lower 2θ angles, due to an increase of interplanar distances (d) changing from 7.38 Å and 4.92–7.52 Å and 4.99 Å for a and b axes, respectively (Fig. 7a and S9).

Table 1 reports the crystallinity degree (X_c) of both bare and treated LLDPE samples evaluated as described in Section 2, and the mean size of crystallites (D) determined by Scherrer equation. The increase of both D

Table 1
Values of crystallite sizes, D, crystalline indexes, X_c and carbonyl index, C.I., of LLDPE samples before and after the treatment with T-*Abi*.

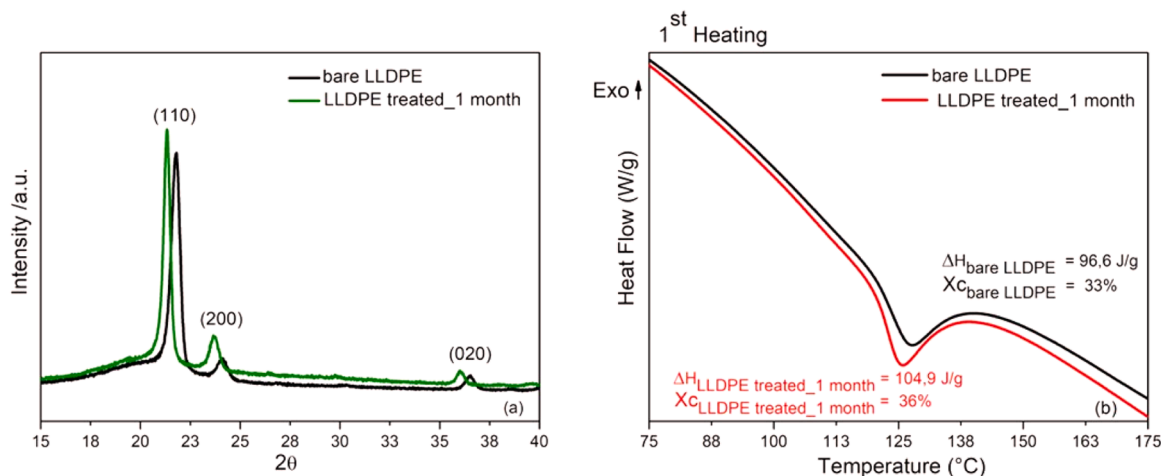| Sample	D_{110} (Å)	D_{200} (Å)	D_{020} (Å)	X_c (%) *X-ray analysis*	X_c (%) *Thermal analysis*	Carbonyl Index, C.I.
Bare LLDPE	156	105	126	34	33	0.040
LLDPE treated 1 month	217	141	171	39	36	0.13

Fig. 7. a) XRD spectra of bare LLDPE and LLDPE treated with T-*Abi* for 1 month and b) Thermograms for bare LLDPE and LLDPE treated with T-*Abi* for 1 month (first heating).

and X_c values sheds some light on the degradation mechanism of LLDPE. T-*Abi* is responsible for the oxidative degradation of LLDPE, which results in a secondary crystallization phenomenon and in an increase of the crystal size. More in detail, the action of T-*Abi* makes the polymer chains, in the amorphous region, more mobile and free to further crystallize [93].

To additionally confirm that the degradation mechanism of LLDPE occurs through an increase of its crystallinity degree, DSC measurements were performed on pristine and treated LLDPE samples and the resulting thermograms are shown in Fig. 7b. The enthalpic crystallinity index was estimated for bare and treated LLDPE, together with their melting temperatures (T_m), following the procedure reported in Section 2. As shown in Fig. 7b, the oxidative degradation of LLDPE causes the increase of the enthalpic crystallinity grade, which changes from 33 % to 36 % in agreement with XRD analysis (Table 1) [94]. The degradation of LLDPE exerted by T-*Abi* leads to an increase of the crystallinity degree as well as of the concentration of chemical impurities (i.e., by-products with low molecular weight derived from the degradation process) [30,95], as proved by the slight decrease of the melting temperature from 127.6 °C to 125.6 °C for bare and treated LLDPE, respectively.

To monitor the chemical changes on the film surfaces induced by the treatment in the presence of T-*Abi*, ATR-FTIR spectra of LLDPE samples were recorded, as shown in Fig. S10. Bare LLDPE samples exhibit the following characteristic IR bands: at 3038–2775 cm^{-1} (ν C-H), at 1480–1420 cm^{-1} (δ CH2) and (δ CH3), and at 740–700 cm^{-1} (ρ CH2) [96]. These typical peaks can still be found in the ATR-FTIR spectra of LLDPE treated with T-*Abi* and sampled at the different times. In this case, ATR-FTIR analysis demonstrated the appearance of new significant IR bands during the treatment, already after 4 days. Indeed, *i)* a broad band in the range 3600–3200 cm^{-1} (ν OH), ascribable to the presence of hydrogen-bonded products, such as hydroperoxides or alcohols; *ii)* a small band in the range 1700–1500 cm^{-1} (ν C=O), the intensity of which increases slightly over the time [30] and *iii)* two peaks, the first in the range (1237 cm^{-1}-1210 cm^{-1}) and the second at 1150 cm^{-1}. The appearance of the band related to carbonyl group was widely associated in literature [97,98] to the surface oxidation extent of microplastics, and the related carbonyl index (CI) was evaluated and displayed in Table 1. It should be noted that, recently, the CI index was adopted as a method to estimate the degradation efficiency of LDPE films [62]. Even if it is not easy to compare our results with the ones obtained under UV exposure, the observed CI increase appears significant considering that it was obtained in absence of any direct illumination source. The highest IR bands appearing during the degradation of LLDPE films, occurred in the range (1237–1150) cm^{-1}, assigned to polytetrafluoroethylene (PTFE) [99] highlight that the exploited oxidative mechanism may also slightly alter the backbone of materials like PTFE, generally recognized as chemically resistant and inert. Based on that, it seems that the treatment of LLDPE samples with T-*Abi* may induce an exfoliation of PTFE from the virgin magnetic stir bar used during the experiments, as already observed in a recent study [100].

4. Conclusions

Following a waste-to-wealth approach, a new hybrid gel-derived material was synthesized using a rosin bio-waste, mainly composed of abietic acid. A simple, green and sustainable sol-gel synthesis procedure enabled the utilization of rosin without any costly and time-consuming chemical transformations. In the resulting TiO_2-abietate material, the bio-waste compound acts as ligand to Ti^{4+} ions forming a ligand-to-metal charge transfer complex, as predicted by DFT calculations and then assessed by XPS, FTIR and DRUV analyses. This complex plays a key role in the spontaneous generation of superoxide radical ions on the hybrid surface, without requiring any energy source. These radicals remain stable at indirect daylight and room temperature, as ascertained by EPR spectroscopy, which makes this material a powerful green tool for oxidative degradation processes. Its effectiveness in the degradation

of LLDPE microplastics under indoor light was assessed in aqueous suspension, observing impressive results within one month. Degradation by-products, namely alkanes, alcohols and esters, were identified in solution by GC-MS. Physicochemical analyses of treated LLDPE films also confirmed its degradation, indicated by an increase of carbonyl index and crystallinity. The chemical characterization elucidates that LLDPE undergoes a secondary crystallization mechanism and a partial surface oxidation, including the break of polymer chains. The observed modifications, induced by the presence of the hybrid material without direct external energy inputs, allowed to propose an exemplificative degradation mechanism that differs from that reported in the literature for the photoinitiated oxidative degradation. Overall, our study shows a viable way to face the global problem caused by the new ubiquitous pollutant represented by microplastics. In the future, this type of lab-scale process could be optimized to be employed in chemical recycling strategies, fostering the development of a circular approach in the field of waste management.

Environmental implication

Herein we propose an innovative strategy to face the current issue of microplastics. Microplastics are a potentially hazardous material as they can enter the food chain and act as carriers of toxic contaminants, due to their small size and large surface area. The model microplastic investigated is LLDPE, widely used in the packaging field and then discharged in the environment. A hybrid TiO_2 synthesized using a waste natural resin as component without any chemical modification induced the oxidative degradation of LLDPE under indirect daylight, as indicated by the by-products formed and the increase of carbonyl index and crystallinity.

CRediT authorship contribution statement

Paola Amato: Data curation, Writing- Original draft preparation, Investigation, Formal Analysis. **Marzia Fantauzzi:** Investigation, Formal Analysis, Writing- Original draft preparation. **Filomena Sannino:** Supervision, Writing- Reviewing and Editing. **Ida Ritacco:** Writing- Original draft preparation, Formal Analysis, Data Curation, Investigation. **Giuseppe Santoriello:** Formal Analysis, Data Curation. **Matteo Farnesi Camellone:** Formal Analysis, Data Curation. **Claudio Imparato:** Conceptualization, Writing- Reviewing and Editing. **Aurelio Bifulco:** Conceptualization, Writing- Reviewing and Editing. **Giuseppe Vitiello:** Formal analysis, Supervision. **Lucia Caporaso:** Supervision, Writing- Reviewing and Editing. **Antonella Rossi:** Supervision, Writing- Reviewing and Editing. **Antonio Aronne:** Conceptualization, Supervision, Writing- Reviewing and Editing.

Declaration of Competing Interest

The authors declare that they have no known competing financial interests or personal relationships that could have appeared to influence the work reported in this paper.

Data availability

The data that has been used is confidential.

Appendix A. Supporting information

Supplementary data associated with this article can be found in the online version at doi:10.1016/j.jhazmat.2023.132907.

References

[1] Gu, Y., Zhao, J., Johnson, J.A., 2020. Polymer networks: from plastics and gels to porous frameworks. Angew Chem - Int Ed 59, 5022–5049. https://doi.org/10.1002/anie.201902900.

[2] Lin, Z., Jin, T., Zou, T., Xu, L., Xi, B., Xu, D., et al., 2022. Current progress on plastic/microplastic degradation: fact influences and mechanism. Environ Pollut 304. https://doi.org/10.1016/j.envpol.2022.119159.

[3] Jaiswal, P.B., Pushkar, B.K., Maikap, K., Mahanwar, P.A., 2022. Abiotic aging assisted bio-oxidation and degradation of LLDPE/LDPE packaging polyethylene film by stimulated enrichment culture. Polym Degrad Stab 206, 110156. https://doi.org/10.1016/j.polymdegradstab.2022.110156.

[4] Hou, Q., Zhen, M., Qian, H., Nie, Y., Bai, X., Xia, T., et al., 2021. Upcycling and catalytic degradation of plastic wastes. Cell Rep Phys Sci 2, 100514. https://doi.org/10.1016/j.xcrp.2021.100514.

[5] Awoyera, P.O., Adesina, A., 2020. Plastic wastes to construction products: status, limitations and future perspective. Case Stud Constr Mater 12, e00330. https://doi.org/10.1016/j.cscm.2020.e00330.

[6] Huang, D., Tao, J., Cheng, M., Deng, R., Chen, S., Yin, L., et al., 2021. Microplastics and Nanoplastics in the Environment: Macroscopic Transport and Effects on Creatures. Elsevier,. https://doi.org/10.1016/j.jhazmat.2020.124399.

[7] Sharma, S., Basu, S., Shetti, N.P., Nadagouda, M.N., Aminabhavi, T.M., 2021. Microplastics in the environment: occurrence, perils, and eradication. Chem Eng J 408, 127317. https://doi.org/10.1016/j.cej.2020.127317.

[8] Liu, M., Lu, S., Song, Y., Lei, L., Hu, J., Lv, W., et al., 2018. Microplastic and mesoplastic pollution in farmland soils in suburbs of Shanghai, China. Environ Pollut 242, 855–862. https://doi.org/10.1016/j.envpol.2018.07.051.

[9] Zhou, D., Chen, J., Wu, J., Yang, J., Wang, H., 2021. Biodegradation and catalytic-chemical degradation strategies to mitigate microplastic pollution. Sustain Mater Technol 28, e00251. https://doi.org/10.1016/j.susmat.2021.e00251.

[10] Zhao, J., Ran, W., Teng, J., Liu, Y., Liu, H., Yin, X., et al., 2018. Microplastic pollution in sediments from the Bohai Sea and the Yellow Sea, China. Sci Total Environ 640–641, 637–645. https://doi.org/10.1016/j.scitotenv.2018.05.346.

[11] Zhang, Y., Kang, S., Allen, S., Allen, D., Gao, T., Sillanpää, M., 2020. Atmospheric microplastics: a review on current status and perspectives. Earth-Sci Rev 203, 103118. https://doi.org/10.1016/j.earscirev.2020.103118.

[12] Wang, S., Chen, H., Zhou, X., Tian, Y., Lin, C., Wang, W., et al., 2020. Microplastic abundance, distribution and composition in the mid-west Pacific Ocean. Environ Pollut 264, 114125. https://doi.org/10.1016/j.envpol.2020.114125.

[13] Deng, H., Wei, R., Luo, W., Hu, L., Li, B., Di, Y., et al., 2020. Microplastic pollution in water and sediment in a textile industrial area. Environ Pollut 258, 113658. https://doi.org/10.1016/j.envpol.2019.113658.

[14] Zhou, B., Wang, J., Zhang, H., Shi, H., Fei, Y., Huang, S., et al., 2020. Microplastics in agricultural soils on the coastal plain of Hangzhou Bay, east China: multiple sources other than plastic mulching film. J Hazard Mater 388, 121814. https://doi.org/10.1016/j.jhazmat.2019.121814.

[15] Dris, R., Gasperi, J., Mirande, C., Mandin, C., Guerrouache, M., Langlois, V., et al., 2017. A first overview of textile fibers, including microplastics, in indoor and outdoor environments. Environ Pollut 221, 453–458. https://doi.org/10.1016/j.envpol.2016.12.013.

[16] Klein, M., Fischer, E.K., 2019. Microplastic abundance in atmospheric deposition within the Metropolitan area of Hamburg, Germany. Sci Total Environ 685, 96–103. https://doi.org/10.1016/j.scitotenv.2019.05.405.

[17] Krause, S., Baranov, V., Nel, H.A., Drummond, J.D., Kukkola, A., Hoellein, T., et al., 2021. Gathering at the top? Environmental controls of microplastic uptake and biomagnification in freshwater food webs. Environ Pollut 268, 115750. https://doi.org/10.1016/j.envpol.2020.115750.

[18] Turner, A., 2016. Heavy metals, metalloids and other hazardous elements in marine plastic litter. Mar Pollut Bull 111, 136–142. https://doi.org/10.1016/j.marpolbul.2016.07.020.

[19] Jia, Y.W., Huang, Z., Hu, L.X., Liu, S., Li, H.X., Li, J.L., et al., 2020. Occurrence and mass loads of biocides in plastic debris from the Pearl River system, South China. Chemosphere 246, 125771. https://doi.org/10.1016/j.chemosphere.2019.125771.

[20] Du, H., Xie, Y., Wang, J., 2021. Microplastic degradation methods and corresponding degradation mechanism: research status and future perspectives. J Hazard Mater 418, 126377. https://doi.org/10.1016/j.jhazmat.2021.126377.

[21] Chen, J., Wu, J., Sherrell, P.C., Chen, J., Wang, H., Xian Zhang, W., et al., 2022. How to build a microplastics-free environment: strategies for microplastics degradation and plastics recycling. Adv Sci 9, 1–36. https://doi.org/10.1002/advs.202103764.

[22] Cholewinski, A., Dadzie, E., Sherlock, C., Anderson, W.A., Charles, T.C., Habib, K., et al., 2022. A critical review of microplastic degradation and material flow analysis towards a circular economy. Environ Pollut 315, 120334. https://doi.org/10.1016/j.envpol.2022.120334.

[23] Tian, W., Song, P., Zhang, H., Duan, X., Wei, Y., Wang, H., et al., 2023. Microplastic materials in the environment: problem and strategical solutions. Prog Mater Sci 132, 101035. https://doi.org/10.1016/j.pmatsci.2022.101035.

[24] Zhao, G., Zou, J., Chen, X., Liu, L., Wang, Y., Zhou, S., et al., 2021. Iron-based catalysts for persulfate-based advanced oxidation process: microstructure, property and tailoring. Chem Eng J 421, 127845. https://doi.org/10.1016/j.cej.2020.127845.

[25] Giannakis, S., Lin, K.Y.A., Ghanbari, F., 2021. A review of the recent advances on the treatment of industrial wastewaters by sulfate radical-based advanced oxidation processes (SR-AOPs). Chem Eng J 406, 127083. https://doi.org/10.1016/j.cej.2020.127083.

[26] Chen, Y., Chen, H., Li, J., Xiao, L., 2019. Rapid and efficient activated sludge treatment by electro-Fenton oxidation. Water Res 152, 181–190. https://doi.org/10.1016/j.watres.2018.12.035.

[27] Moreira, F.C., Boaventura, R.A.R., Brillas, E., Vilar, V.J.P., 2017. Electrochemical advanced oxidation processes: a review on their application to synthetic and real wastewaters. Appl Catal B Environ 202, 217–261. https://doi.org/10.1016/j.apcatb.2016.08.037.

[28] Ariza-Tarazona, M.C., Villarreal-Chiu, J.F., Hernández-López, J.M., Rivera De la Rosa, J., Barbieri, V., Siligardi, C., et al., 2020. Microplastic pollution reduction by a carbon and nitrogen-doped TiO2: Effect of pH and temperature in the photocatalytic degradation process. J Hazard Mater 395, 122632. https://doi.org/10.1016/j.jhazmat.2020.122632.

[29] Nabi, I., Bacha, A.U.R., Li, K., Cheng, H., Wang, T., Liu, Y., et al., 2020. Complete photocatalytic mineralization of microplastic on TiO2 nanoparticle film. IScience 23, 101326. https://doi.org/10.1016/j.isci.2020.101326.

[30] Amato, P., Muscetta, M., Venezia, V., Cocca, M., Gentile, G., Castaldo, R., et al., 2023. Eco-sustainable design of humic acids-doped ZnO nanoparticles for UVA/light photocatalytic degradation of LLDPE and PLA plastics. J Environ Chem Eng 11, 109003. https://doi.org/10.1016/j.jece.2022.109003.

[31] Ghatge, S., Yang, Y., Ko, Y., Yoon, Y., Ahn, J.H., Kim, J.J., et al., 2022. Degradation of sulfonated polyethylene by a bio-photo-fenton approach usingglucose oxidase immobilized on titanium dioxide. J Hazard Mater 423, 127067. https://doi.org/10.1016/j.jhazmat.2021.127067.

[32] Liu, B., Jiang, Q., Qiu, Z., Liu, L., Wei, R., Zhang, X., et al., 2022. Process analysis of microplastic degradation using activated PMS and Fenton reagents. Chemosphere 298, 134220. https://doi.org/10.1016/j.chemosphere.2022.134220.

[33] Venezia, V., Verrillo, M., Gallucci, N., Di Girolamo, R., Luciani, G., D'Errico, G., et al., 2023. Exploiting bioderived humic acids: a molecular combination with ZnO nanoparticles leads to nanostructured hybrid interfaces with enhanced pro-oxidant and antibacterial activity. J Environ Chem Eng 11, 108973. https://doi.org/10.1016/j.jece.2022.108973.

[34] Silva, A.B., Costa, M.F., Duarte, A.C., 2018. Biotechnology advances for dealing with environmental pollution by micro(nano)plastics: lessons on theory and practices. Curr Opin Environ Sci Heal 1, 30–35. https://doi.org/10.1016/j.coesh.2017.10.005.

[35] Auta, H.S., Emenike, C.U., Fauziah, S.H., 2017. Screening of Bacillus strains isolated from mangrove ecosystems in Peninsular Malaysia for microplastic degradation. Environ Pollut 231, 1552–1559. https://doi.org/10.1016/j.envpol.2017.09.043.

[36] Goel, V., Luthra, P., Kapur, G.S., Ramakumar, S.S.V., 2021. Biodegradable/bio-plastics: myths and realities. J Polym Environ 29, 3079–3104. https://doi.org/10.1007/s10924-021-02099-1.

[37] Miao, Y., von Jouanne, A., Yokochi, A., 2021. Current technologies in depolymerization process and the road ahead. Polymers 13, 1–17. https://doi.org/10.3390/polym13030449.

[38] Wu Klingler, W., Bifulco, A., Polisi, C., Huang, Z., Gaan, S., 2023. Recyclable inherently flame-retardant thermosets: chemistry, properties and applications. Compos Part B Eng 258, 110667. https://doi.org/10.1016/j.compositesb.2023.110667.

[39] Martín, A.J., Mondelli, C., Jaydev, S.D., Pérez-Ramírez, J., 2021. Catalytic processing of plastic waste on the rise. Chem 7, 1487–1533. https://doi.org/10.1016/j.chempr.2020.12.006.

[40] Korley, L.T.J., Epps, T.H., Helms, B.A., Ryan, A.J., 2021. Toward polymer upcycling-adding value and tackling circularity. Science 69, 66–69.

[41] Thiounn, T., Smith, R.C., 2020. Advances and approaches for chemical recycling of plastic waste. J Polym Sci 58, 1347–1364. https://doi.org/10.1002/pol.20190261.

[42] Huang, Z., Shanmugam, M., Liu, Z., Brookfield, A., Bennett, E.L., Guan, R., et al., 2022. Chemical recycling of polystyrene to valuable chemicals via selective acid-catalyzed aerobic oxidation under visible light. J Am Chem Soc 144, 6532–6542. https://doi.org/10.1021/jacs.2c01410.

[43] Pirozzi, D., Imparato, C., D'Errico, G., Vitiello, G., Aronne, A., Sannino, F., 2020. Three-year lifetime and regeneration of superoxide radicals on the surface of hybrid TiO2 materials exposed to air. J Hazard Mater 387. https://doi.org/10.1016/j.jhazmat.2019.121716.

[44] Sannino, F., Pernice, P., Imparato, C., Aronne, A., D'Errico, G., Minieri, L., et al., 2015. Hybrid TiO2-acetylacetonate amorphous gel-derived material with stably adsorbed superoxide radical active in oxidative degradation of organic pollutants. RSC Adv 5, 93831–93839. https://doi.org/10.1039/c5ra21176j.

[45] Ritacco, I., Imparato, C., Falivene, L., Cavallo, L., Magistrato, A., Caporaso, L., et al., 2021. Spontaneous production of ultrastable reactive oxygen species on titanium oxide surfaces modified with organic ligands. Adv Mater Interfaces 8. https://doi.org/10.1002/admi.202100629.

[46] Imparato, C., D'Errico, G., Macyk, W., Kobielusz, M., Vitiello, G., Aronne, A., 2022. Interfacial charge transfer complexes in TiO2-enediol hybrids synthesized by sol-gel. Langmuir 38, 1821–1832. https://doi.org/10.1021/acs.langmuir.1c02939.

[47] Muñoz-García, A.B., Sannino, F., Vitiello, G., Pirozzi, D., Minieri, L., Aronne, A., et al., 2015. Origin and electronic features of reactive oxygen species at hybrid zirconia-acetylacetonate interfaces. ACS Appl Mater Interfaces 7, 21662–21667. https://doi.org/10.1021/acsami.5b06988.

[48] Perdew, J.P., Burke, K., Ernzerhof, M., Perdew, Burke, Ernzerhof, Reply, 1998. Phys Rev Lett 80, 891. https://doi.org/10.1103/PhysRevLett.80.891.

[49] Giannozzi, P., Andreussi, O., Brumme, T., Bunau, O., Nardelli, M.B., Calandra, M., et al., 2017. Advanced capabilities for materials modelling with Quantum ESPRESSO. (arXiv:1709.10010v1 [cond-mat.mtrl-sci]). J Phys Condens Matter 29, 465901. ⟨http://arxiv.org/abs/1709.10010⟩.

[50] Setvin, M., Shi, X., Hulva, J., Simschitz, T., Parkinson, G.S., Schmid, M., et al., 2017. Methanol on anatase TiO2 (101): mechanistic insights into photocatalysis. ACS Catal 7, 7081–7091. https://doi.org/10.1021/acscatal.7b02003.

[51] Kowalski, P.M., Camellone, M.F., Nair, N.N., Meyer, B., Marx, D., 2010. Charge localization dynamics induced by oxygen vacancies on the TiO 2(110) surface. Phys Rev Lett 105, 5–8. https://doi.org/10.1103/PhysRevLett.105.146405.

[52] Ritacco, I., Sacco, O., Caporaso, L., Camellone, M.F., 2022. DFT investigation of Substitutional and Interstitial Nitrogen-Doping Effects on a ZnO(100)-TiO2(101) Heterojunction. J Phys Chem C 126, 3180–3193. https://doi.org/10.1021/acs.jpcc.1c09395.

[53] Navarra, W., Ritacco, I., Sacco, O., Caporaso, L., Farnesi Camellone, M., Venditto, V., et al., 2022. Density functional theory study and photocatalytic activity of ZnO/N-doped TiO2 heterojunctions. J Phys Chem C 126, 7000–7011. https://doi.org/10.1021/acs.jpcc.2c00152.

[54] Finkelstein-Shapiro, D., Davidowski, S.K., Lee, P.B., Guo, C., Holland, G.P., Rajh, T., et al., 2016. Direct evidence of chelated geometry of catechol on TiO2 by a combined solid-state NMR and DFT study. J Phys Chem C 120, 23625–23630. https://doi.org/10.1021/acs.jpcc.6b08041.

[55] Liu, L.M., Li, S.C., Cheng, H., Diebold, U., Selloni, A., 2011. Growth and organization of an organic molecular monolayer on TiO 2: Catechol on anatase (101). J Am Chem Soc 133, 7816–7823. https://doi.org/10.1021/ja200001r.

[56] Tang, W., Sanville, E., Henkelman, G., 2009. A grid-based Bader analysis algorithm without lattice bias. J Phys Condens Matter 21. https://doi.org/10.1088/0953-8984/21/8/084204.

[57] Henkelman, G., Arnaldsson, A., Jónsson, H., 2006. A fast and robust algorithm for Bader decomposition of charge density. Comput Mater Sci 36, 354–360. https://doi.org/10.1016/j.commatsci.2005.04.010.

[58] Grimme, S., Antony, J., Ehrlich, S., Krieg, H., 2010. A consistent and accurate ab initio parametrization of density functional dispersion correction (DFT-D) for the 94 elements H-Pu. J Chem Phys 132. https://doi.org/10.1063/1.3382344.

[59] Fairley, N., Fernandez, V., Richard-Plouet, M., Guillot-Deudon, C., Walton, J., Smith, E., et al., 2021. Systematic and collaborative approach to problem solving using X-ray photoelectron spectroscopy. Appl Surf Sci Adv 5, 100112. https://doi.org/10.1016/j.apsadv.2021.100112.

[60] Matthew, J., 2003. In: Briggs, D., Grant, J.T. (Eds.), Surface Analysis by Auger and x-ray Photoelectron Spectroscopy. IMPublications, Chichester, UK and SurfaceSpectra, Manchester, UK, p. 900 pp., ISBN 1-901019-04-7, 900 pp, Surf. Interface Anal. 36 (2004). ⟨https://doi.org/10.1002/sia.2005⟩.

[61] Wunderlich, B., Czornyj, G., 1977. A study of equilibrium melting of polyethylene. Macromolecules 10, 906–913. https://doi.org/10.1021/ma60059a006.

[62] Kaewkam, P., Kanchanapaetnukul, A., Khamyan, J., Phadmanee, N., Lin, K.Y.A., Kobwittaya, K., et al., 2022. UV-assisted TiO2photocatalytic degradation of virgin LDPE films: effect of UV-A, UV-C, and TiO2. J Environ Chem Eng 10. https://doi.org/10.1016/j.jece.2022.108131.

[63] Hsu, Y.C., Weir, M.P., Truss, R.W., Garvey, C.J., Nicholson, T.M., Halley, P.J., 2012. A fundamental study on photo-oxidative degradation of linear low density polyethylene films at embrittlement. Polymers 53, 2385–2393. https://doi.org/10.1016/j.polymer.2012.03.044.

[64] Lee, C.M., Lim, S., Kim, G.Y., Kim, D., Kim, D.W., Lee, H.C., et al., 2004. Rosin microparticles as drug carriers: influence of various solvents on the formation of particles and sustained-release of indomethacin. Biotechnol Bioprocess Eng 9, 476–481. https://doi.org/10.1007/BF02933489.

[65] Atzei, D., Fantauzzi, M., Rossi, A., Fermo, P., Piazzalunga, A., Valli, G., et al., 2014. Surface chemical characterization of PM 10 samples by XPS. Appl Surf Sci 307, 120–128. https://doi.org/10.1016/j.apsusc.2014.03.178.

[66] Beamson, G., Briggs, D., 1993. High resolution XPS of organic polymers: the scienta ESCA300 database. J Chem Educ 70, A25. https://doi.org/10.1021/ed070pA25.5.

[67] Mangolini, F., Rossi, A., Spencer, N.D., 2011. Chemical reactivity of triphenyl phosphorothionate (TPPT) with iron: an ATR/FT-IR and XPS investigation. J Phys Chem C 115, 1339–1354. https://doi.org/10.1021/jp107617d.

[68] Beltran, V., Salvadó, N., Butí, S., Pradell, T., 2016. Ageing of resin from Pinus species assessed by infrared spectroscopy. Anal Bioanal Chem 408, 4073–4082. https://doi.org/10.1007/s00216-016-9496-x.

[69] Ren, F., Zheng, Y.F., Liu, X.M., Yue, X.Y., Ma, L., Li, W.G., et al., 2015. An investigation of the oxidation mechanism of abietic acid using two-dimensional infrared correlation spectroscopy. J Mol Struct 1084, 236–243. https://doi.org/10.1016/j.molstruc.2014.12.055.

[70] Zumbühl, S., Brändle, A., Hochuli, A., Scherrer, N.C., Caseri, W., 2017. Derivatization technique to identify specifically carbonyl groups by infrared spectroscopy: characterization of photooxidative aging products in terpenes and terpeneous resins. Anal Chem 89, 1742–1748. https://doi.org/10.1021/acs.analchem.6b04008.

[71] He, Y., Dulub, O., Cheng, H., Selloni, A., Diebold, U., 2009. Evidence for the predominance of subsurface defects on reduced anatase TiO2(101). Phys Rev Lett 102, 1–4. https://doi.org/10.1103/PhysRevLett.102.106105.

[72] Aronne, A., Fantauzzi, M., Imparato, C., Atzei, D., De Stefano, L., D'Errico, G., et al., 2017. Electronic properties of TiO2-based materials characterized by high Ti3+ self-doping and low recombination rate of electron-hole pairs. RSC Adv 7, 2373–2381. https://doi.org/10.1039/c6ra27111a.

[73] Tang, H., Berger, H., Schmid, P.E., Lévy, F., Burri, G., 1993. Photoluminescence in TiO2 anatase single crystals. Solid State Commun 87, 847–850. https://doi.org/10.1016/0038-1098(93)90427-O.

[74] Berger, T., Sterrer, M., Diwald, O., Knözinger, E., Panayotov, D., Thompson, T.L., et al., 2005. Light-induced charge separation in anatase TiO 2 particles. J Phys Chem B 109, 6061–6068. https://doi.org/10.1021/jp0404293.

[75] Halwidl, D., Mayr-Schmölzer, W., Setvin, M., Fobes, D., Peng, J., Mao, Z., et al., 2018. A full monolayer of superoxide: oxygen activation on the unmodified Ca3Ru2O7(001) surface. J Mater Chem A 6, 5703–5713. https://doi.org/10.1039/c8ta00265g.

[76] Aschauer, U., Chen, J., Selloni, A., 2010. Peroxide and superoxide states of adsorbed O2 on anatase TiO 2 (101) with subsurface defects. Phys Chem Chem Phys 12, 12956–12960. https://doi.org/10.1039/c0cp00116c.

[77] Li, Y.F., Aschauer, U., Chen, J., Selloni, A., 2014. Adsorption and reactions of O2 on anatase TiO2. Acc Chem Res 47, 3361–3368. https://doi.org/10.1021/ar400312t.

[78] Aronne, A., Sannino, F., Bonavolontà, S.R., Fanelli, E., Mingione, A., Pernice, P., et al., 2012. Use of a new hybrid sol-gel zirconia matrix in the removal of the herbicide MCPA: a sorption/degradation process. Environ Sci Technol 46, 1755–1763. https://doi.org/10.1021/es203223s.

[79] Makuła, P., Pacia, M., Macyk, W., 2018. How to correctly determine the band gap energy of modified semiconductor photocatalysts based on UV-Vis spectra. J Phys Chem Lett 9, 6814–6817. https://doi.org/10.1021/acs.jpclett.8b02892.

[80] Passaro, J., Imparato, C., Parida, D., Bifulco, A., Branda, F., Aronne, A., 2022. Electrospinning of PVP-based ternary composites containing SiO2 nanoparticles and hybrid TiO2 microparticles with adsorbed superoxide radicals. Compos Part B Eng 238, 109874. https://doi.org/10.1016/j.compositesb.2022.109874.

[81] Vitiello, G., Zanfardino, A., Tammaro, O., Di Napoli, M., Caso, M.F., Pezzella, A., et al., 2018. Bioinspired hybrid eumelanin-TiO2 antimicrobial nanostructures: the key role of organo-inorganic frameworks in tuning eumelanin's biocide action mechanism through membrane interaction. RSC Adv 8, 28275–28283. https://doi.org/10.1039/c8ra04315a.

[82] Nosaka, Y., Nosaka, A.Y., 2017. Generation and detection of reactive oxygen species in photocatalysis. Chem Rev 117, 11302–11336. https://doi.org/10.1021/acs.chemrev.7b00161.

[83] Hayyan, M., Hashim, M.A., Alnashef, I.M., 2016. Superoxide ion: generation and chemical implications. Chem Rev 116, 3029–3085. https://doi.org/10.1021/acs.chemrev.5b00407.

[84] De Frond, H., Thornton Hampton, L., Kotar, S., Gesulga, K., Matuch, C., Lao, W., et al., 2022. Monitoring microplastics in drinking water: an interlaboratory study to inform effective methods for quantifying and characterizing microplastics. Chemosphere 298, 134282. https://doi.org/10.1016/j.chemosphere.2022.134282.

[85] Kang, J., Zhou, L., Duan, X., Sun, H., Ao, Z., Wang, S., 2019. Degradation of cosmetic microplastics via functionalized carbon nanosprings. Matter 1, 745–758. https://doi.org/10.1016/j.matt.2019.06.004.

[86] Etacheri, V., Di Valentin, C., Schneider, J., Bahnemann, D., Pillai, S.C., 2015. Visible-light activation of TiO2 photocatalysts: advances in theory and experiments. J Photochem Photobiol C Photochem Rev 25, 1–29. https://doi.org/10.1016/j.jphotochemrev.2015.08.003.

[87] Huang, J., Liu, Y., Lu, L., Li, L., 2012. The photocatalytic properties of amorphous TiO 2 composite films deposited by magnetron sputtering. Res Chem Intermed 38, 487–498. https://doi.org/10.1007/s11164-011-0365-0.

[88] Tofa, T.S., Kunjali, K.L., Paul, S., Dutta, J., 2019. Visible light photocatalytic degradation of microplastic residues with zinc oxide nanorods. Environ Chem Lett 17, 1341–1346. https://doi.org/10.1007/s10311-019-00859-z.

[89] Fotopoulou, K.N., Karapanagioti, H.K., 2019. Degradation of various plastics in the environment. Handb Environ Chem 78, 71–92. https://doi.org/10.1007/698_2017_11.

[90] Gewert, B., Plassmann, M.M., Macleod, M., 2015. Pathways for degradation of plastic polymers floating in the marine environment. Environ Sci Process Impacts 17, 1513–1521. https://doi.org/10.1039/c5em00207a.

[91] Llorente-García, B.E., Hernández-López, J.M., Zaldívar-Cadena, A.A., Siligardi, C., Cedillo-González, E.I., 2020. First insights into photocatalytic degradation of HDPE and LDPE microplastics by a mesoporous N-TiO2 coating: effect of size and shape of microplastics. Coatings 10. https://doi.org/10.3390/coatings10070658.

[92] P. Xvi, P. Ii, P. Laboratorium, T H E Crystal Counter, 42, 1950. 517–527.

[93] Guadagno, L., Naddeo, C., Vittoria, V., Camino, G., Cagnani, C., 2001. Chemical and morphological modifications of irradiated linear low density polyethylene (LLDPE). Polym Degrad Stab 72, 175–186. ⟨www.elsevier.nl/locate/polydegstab⟩.

[94] Nguyen, V.G., Thai, H., Mai, D.H., Tran, H.T., Tran, D.L., Vu, M.T., 2013. Effect of titanium dioxide on the properties of polyethylene/TiO 2 nanocomposites. Compos Part B Eng 45, 1192–1198. https://doi.org/10.1016/j.compositesb.2012.09.058.

[95] Ojeda, T., Freitas, A., Birck, K., Dalmolin, E., Jacques, R., Bento, F., et al., 2011. Degradability of linear polyolefins under natural weathering. Polym Degrad Stab 96, 703–707. https://doi.org/10.1016/j.polymdegradstab.2010.12.004.

[96] Martínez, K.I., González-Mota, R., Soto-Bernal, J.J., Rosales-Candelas, I., 2021. Evaluation by IR spectroscopy of the degradation of different types of commercial polyethylene exposed to UV radiation and domestic compost in ambient conditions. J Appl Polym Sci 138, 6–8. https://doi.org/10.1002/app.50158.

[97] Ali, S.S., Qazi, I.A., Arshad, M., Khan, Z., Voice, T.C., Mehmood, C.T., 2016. Photocatalytic degradation of low density polyethylene (LDPE) films using titania nanotubes. Environ Nanotechnol, Monit Manag 5, 44–53. https://doi.org/10.1016/j.enmm.2016.01.001.

[98] Uheida, A., Mejía, H.G., Abdel-Rehim, M., Hamd, W., Dutta, J., 2021. Visible light photocatalytic degradation of polypropylene microplastics in a continuous water flow system. J Hazard Mater 406, 124299. https://doi.org/10.1016/j.jhazmat.2020.124299.

[99] Hunke, H., Soin, N., Shah, T.H., Kramer, E., Pascual, A., Karuna, M.S.L., et al., 2015. Low-pressure H2, NH3 microwave plasma treatment of polytetrafluoroethylene (PTFE) powders: chemical, thermal and wettability analysis. Materials 8, 2258–2275. https://doi.org/10.3390/ma8052258.

[100] Wang, Y., Zhang, J., Pu, L., Cao, M., Dong, S., Vecitis, C.D., et al., 2022. Unexpected exfoliation and activity of nano poly(tetrafluoroethylene) particles from magnetic stir bars: discovery and implication. Chemosphere 291, 132797. https://doi.org/10.1016/j.chemosphere.2021.132797.